

Cohomological Obstructions to Global Counterfactuals: A Sheaf-Theoretic Foundation for Generative Causal Models

Rui Wu

WURUI22@MAIL.USTC.EDU.CN

School of Management, University of Science and Technology of China
96 Jinzhai Road, Hefei, 230026, Anhui, China

Hong Xie

HONGX87@USTC.EDU.CN

School of Computer Science and Engineering, University of Science and Technology of China
96 Jinzhai Road, Hefei, 230026, Anhui, China

Yongjun Li *

LIONLI@USTC.EDU.CN

School of Management, University of Science and Technology of China
96 Jinzhai Road, Hefei, 230026, Anhui, China

Editor: Action Editor Name

Abstract

Current continuous generative models (e.g., Diffusion Models, Flow Matching) implicitly assume that locally consistent causal mechanisms naturally yield globally coherent counterfactuals. In this paper, we prove that this assumption fails fundamentally when the causal graph exhibits non-trivial homology (e.g., structural conflicts or hidden confounders). We formalize structural causal models as cellular sheaves over Wasserstein spaces, providing a strict algebraic topological definition of cohomological obstructions ($H^1 \neq 0$) in measure spaces. To ensure computational tractability and avoid deterministic singularities (which we define as *manifold tearing*), we introduce entropic regularization and derive the *Entropic Wasserstein Causal Sheaf Laplacian*, a novel system of coupled non-linear Fokker-Planck equations.

Crucially, we prove an entropic pullback lemma for the first variation of pushforward measures. By integrating this with the Implicit Function Theorem (IFT) on Sinkhorn optimality conditions, we establish a direct algorithmic bridge to automatic differentiation (VJP), achieving $\mathcal{O}(1)$ -memory reverse-mode gradients strictly independent of the iteration horizon. Empirically, our framework successfully leverages thermodynamic noise to navigate topological barriers ("entropic tunneling") in high-dimensional scRNA-seq counterfactuals. Finally, we invert this theoretical framework to introduce the Topological Causal Score, demonstrating that our Sheaf Laplacian acts as a highly sensitive algebraic detector for topology-aware causal discovery.

1 Introduction and Motivating Example

Continuous generative models, such as score-based diffusion models and normalizing flows, have demonstrated unprecedented success in counterfactual inference. However, these frameworks implicitly rely on a critical, often unverified hypothesis: that fitting locally consistent causal mechanisms (edges) naturally composes into globally coherent counterfactual distributions over the entire causal graph.

*. Corresponding author.

We reveal that this assumption is fundamentally flawed in the presence of topological obstructions. Consider a simple 3-node directed acyclic graph with paths $A \rightarrow B \rightarrow C$ and $A \rightarrow C$. If the structural equations dictate conflicting mechanisms—for instance, the path through B attempts to push C towards $+4$, while the direct edge $A \rightarrow C$ pulls it towards -4 —the system exhibits a non-trivial homological obstruction.

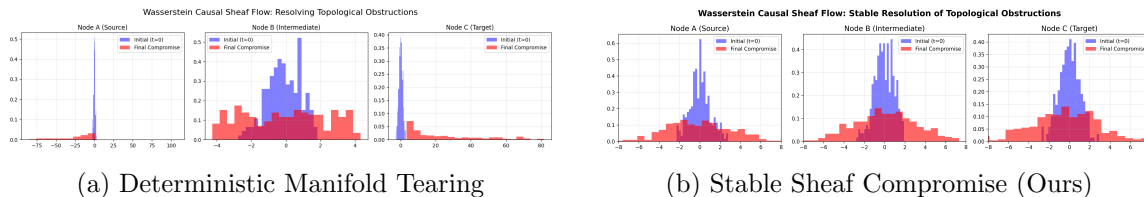


Figure 1: The impact of topological obstructions on causal generative models. (a) Unregularized, deterministic models attempt to resolve the contradiction by pushing probability measures to infinity, resulting in catastrophic manifold tearing. (b) Our proposed Entropic Sheaf Laplacian leverages thermodynamic diffusion to gracefully resolve the conflict, guiding the system to a globally coherent stationary state.

In such geometrically frustrated systems, enforcing deterministic local mechanisms leads to mathematical singularities. As demonstrated in Figure 1(a), unregularized gradient flows attempting to resolve this contradiction experience exponential variance blow-up, tearing the probability manifold apart and sending particles to infinity. We formalize this failure mode as *manifold tearing*.

To resolve this limitation, we bridge Pearl’s causal inference with Grothendieck’s sheaf theory and Otto’s Wasserstein calculus. By modeling the Structural Causal Model (SCM) as a cellular sheaf over Wasserstein spaces and injecting thermodynamic noise (entropic regularization), we derive the *Entropic Wasserstein Causal Sheaf Laplacian*. As shown in Figure 1(b), this novel operator elegantly resolves topological conflicts without deterministic singularities.

2 Related Work

Continuous Causal Generative Models. Recent advancements in generative AI have deeply integrated Pearl’s causality (Pearl, 2009) with continuous generative frameworks, such as Causal Normalizing Flows (Kocaoglu et al., 2018) and Causal Diffusion Models (Goudet et al., 2017). These models typically parameterize the structural equations of a DAG as neural ODEs or SDEs. However, they implicitly rely on the assumption of *perfect local composition*—assuming that matching marginals locally along edges will guarantee a coherent global counterfactual distribution. Our work formally identifies the bottleneck of these approaches: in the presence of unobserved confounders or structural conflicts, this assumption breaks down, leading to what we define as manifold tearing.

Topological Deep Learning and Cellular Sheaves. Topological machine learning has recently gained traction, particularly through the use of Cellular Sheaves in Graph Neural Networks (GNNs) Bodnar et al. (2022); Hansen and Ghrist (2019). By attaching vector spaces (stalks) to nodes and linear transformations (restriction maps) to edges, Sheaf-

GNNs can address over-smoothing and heterophily in discrete graph representations. Our paper profoundly generalizes this paradigm. Instead of finite-dimensional Euclidean stalks, we elevate the algebraic structure to infinite-dimensional absolutely continuous Wasserstein spaces $\mathcal{P}_2(\mathcal{M}_v)$, bridging discrete graph topology with continuous geometric measure theory.

Optimal Transport and Wasserstein Gradient Flows. The adoption of Optimal Transport (OT) (Villani, 2003, 2008) in machine learning has been revolutionized by entropic regularization, which yields the computationally tractable Sinkhorn divergence (Cuturi, 2013; Peyré and Cuturi, 2019). While OT is predominantly deployed as a static loss function for generative matching, we utilize it fundamentally differently: as the rigorous geometric metric defining the coboundary operator within our Tangent Causal Sheaf. Furthermore, rather than relying on heuristic neural updates, we formalize the evolution of counterfactual measures strictly as a metric gradient flow (Jordan et al., 1998; Ambrosio et al., 2005). By exploiting the steady-state optimality conditions of the Sinkhorn dual potentials, we elegantly bridge this continuous measure-theoretic flow with modern reverse-mode automatic differentiation, yielding an exact and highly scalable analytic gradient vector field.

3 Mathematical Preliminaries

To establish a rigorous mathematical foundation for topological obstructions in continuous causal inference, we briefly review the necessary concepts from geometric measure theory (Otto calculus) and algebraic topology (cellular sheaves).

3.1 Wasserstein Geometry and Otto Calculus

Let \mathcal{M} be a smooth, compact Riemannian manifold without boundary. We consider the space of absolutely continuous probability measures with finite second moments, denoted as $\mathcal{P}_2(\mathcal{M})$. Endowed with the 2-Wasserstein distance \mathcal{W}_2 , the space $\mathcal{P}_2(\mathcal{M})$ behaves as an infinite-dimensional pseudo-Riemannian manifold Villani (2003).

According to Otto’s geometric calculus, the tangent space at a sufficiently regular measure $\mu \in \mathcal{P}_2(\mathcal{M})$ is formally defined as the closure of the gradients of smooth functions, equipped with the weighted $L^2(\mu)$ inner product:

$$T_\mu \mathcal{P}_2(\mathcal{M}) = \overline{\{\nabla \phi \mid \phi \in C_c^\infty(\mathcal{M})\}}^{L^2(\mu)}, \quad \langle \nabla \phi, \nabla \psi \rangle_\mu = \int_{\mathcal{M}} \langle \nabla \phi, \nabla \psi \rangle_g d\mu. \quad (1)$$

Absolutely continuous curves μ_t in $\mathcal{P}_2(\mathcal{M})$ correspond to velocity vector fields $v_t \in T_{\mu_t} \mathcal{P}_2(\mathcal{M})$ governing the continuity equation $\partial_t \mu_t + \nabla \cdot (v_t \mu_t) = 0$ in the weak sense.

3.2 Regularity Assumptions

To ensure the well-posedness of the ensuing measure-theoretic calculus and partial differential equations, we establish the following foundational regularity assumption, which naturally holds in standard generative modeling settings (e.g., image generation over bounded pixel spaces).

Assumption 1 (Regularity of the Factual Manifold and Mechanisms) *We strictly assume that:*

1. **Compactness:** For each node $v \in \mathcal{V}$, the state space \mathcal{M}_v is a smooth, compact Riemannian manifold without boundary (or the probability measures are strictly supported within a compact geometric domain). This ensures that the Wasserstein spaces $\mathcal{P}_2(\mathcal{M}_v)$ are compact under the weak topology.
2. **Lipschitz Mechanisms:** The deterministic structural equations $\Phi_{uv} : \mathcal{M}_u \rightarrow \mathcal{M}_v$ are bi-Lipschitz diffeomorphisms, ensuring that the pushforward operations preserve absolute continuity.

Remark 1 (Relaxation of Bi-Lipschitz Diffeomorphisms in Deep Learning) While Assumption 1 strictly requires the causal mechanisms Φ_{uv} to be bi-Lipschitz diffeomorphisms, this is naturally satisfied—or rigorously soft-relaxed—in modern deep learning architectures via two complementary avenues:

1. Architectural Realization via Residual Flows: If the structural equation Φ_{uv} is parameterized as a Residual Network, $\Phi_{uv}(x) = x + g_\theta(x)$, and we enforce Spectral Normalization such that the Lipschitz constant $\text{Lip}(g_\theta) < 1$, then by the Banach Fixed-Point Theorem, Φ_{uv} is strictly globally invertible and bi-Lipschitz. Furthermore, employing smooth, non-saturating activation functions (e.g., GELU or Swish) ensures that Φ_{uv} is a valid C^1 -diffeomorphism. This establishes a direct isomorphism between our causal mechanisms and continuous Normalizing Flows (Neural ODEs), where the Picard-Lindelöf theorem guarantees the existence and uniqueness of solutions for Lipschitz continuous vector fields, and the resulting flow map is a valid C^1 -diffeomorphism over the compact state space defined in Assumption 1.

2. Measure-Theoretic Softening via Entropic Regularization: Even if we relax the assumption such that Φ_{uv} is merely a standard Feed-Forward Network (which may fold space and lose injectivity, retaining only a finite global Lipschitz continuity), our framework remains completely rigorous due to the Entropic Regularization ($\varepsilon > 0$).

For unregularized Optimal Transport ($\varepsilon = 0$), the lack of strict convexity in Φ_{uv} would yield a non-differentiable Brenier potential, breaking the geometric pullback in Lemma 4. However, under Sinkhorn regularization, the optimal dual potential $g^{(\varepsilon)}$ is strictly defined via the integral equation $g^{(\varepsilon)}(y) = -\varepsilon \log \int \exp\left(\frac{f^{(\varepsilon)}(x) - c(x,y)}{\varepsilon}\right) d\mu(x)$. Because the cost function $c(x, y) = \|x - y\|^2$ is smooth, the exponential convolution acts as an infinite-dimensional mollifier Peyré and Cuturi (2019), guaranteeing that $g^{(\varepsilon)} \in C^\infty(\mathcal{M}_v)$ and is globally Lipschitz.

By Rademacher’s Theorem, any globally Lipschitz neural network Φ_{uv} is differentiable almost everywhere (a.e.) with respect to the Lebesgue measure. Since our probability measures μ are absolutely continuous, the intersection of the non-differentiable set of Φ_{uv} and the support of μ has measure zero. Consequently, the chain rule strictly holds μ -a.e., and the topological stress vector field $\nabla(g^{(\varepsilon)} \circ \Phi_{uv}) = (J_{\Phi_{uv}})^T \nabla g^{(\varepsilon)}$ is well-defined, bounded, and $L^2(\mu)$ -integrable. Thus, thermodynamic noise ($\varepsilon > 0$) strictly resolves the measure-theoretic singularities introduced by non-invertible neural networks.

3.3 Cellular Sheaves and Cohomology

A cellular sheaf \mathcal{F} over a directed graph $\mathcal{G} = (\mathcal{V}, \mathcal{E})$ assigns a vector space (the stalk) $\mathcal{F}(v)$ to each node $v \in \mathcal{V}$, and a linear transformation (the restriction map) $\mathcal{F}(u \rightarrow e) : \mathcal{F}(u) \rightarrow \mathcal{F}(e)$

for each incident node-edge pair. The space of 0-cochains is $\mathcal{C}^0(\mathcal{G}, \mathcal{F}) = \bigoplus_{v \in \mathcal{V}} \mathcal{F}(v)$, and 1-cochains is $\mathcal{C}^1(\mathcal{G}, \mathcal{F}) = \bigoplus_{e \in \mathcal{E}} \mathcal{F}(e)$.

The linear coboundary operator $d_0 : \mathcal{C}^0 \rightarrow \mathcal{C}^1$ computes local discrepancies across edges. The first cohomology group, characterizing the global topological obstructions (cycles that are not boundaries), is defined algebraically as the quotient space $H^1(\mathcal{G}, \mathcal{F}) = \text{Ker}(d_1)/\text{Im}(d_0)$.

4 The Entropic Causal Sheaf and Topological Linearization

Let $\mathcal{G} = (\mathcal{V}, \mathcal{E})$ be a directed acyclic graph representing the structural causal mechanisms. To elevate causal inference from discrete scalar variables to continuous high-dimensional manifolds, we formalize the Structural Causal Model (SCM) using topological sheaf theory over measure spaces.

4.1 Stalks, Restriction Maps, and Metric Sheaf Discrepancy

For each node $v \in \mathcal{V}$, we assign a *stalk* defined as the non-linear Wasserstein space $\mathcal{P}_2(\mathcal{M}_v)$, acting as the local universe of counterfactual distributions. The *restriction map* for an edge $e = (u, v) \in \mathcal{E}$ is defined as the pushforward operator $\Phi_{uv\#} : \mathcal{P}_2(\mathcal{M}_u) \rightarrow \mathcal{P}_2(\mathcal{M}_v)$, where Φ_{uv} is the deterministic local causal mechanism.

Let $\mathcal{C}^0 = \prod_{v \in \mathcal{V}} \mathcal{P}_2(\mathcal{M}_v)$ denote the base space of 0-cochains, representing a joint assignment of counterfactual marginals $\boldsymbol{\mu} = (\mu_v)_{v \in \mathcal{V}}$. Unlike classical sheaves over vector spaces, the base space \mathcal{C}^0 is a curved metric space lacking a linear group structure. Therefore, we measure local topological friction smoothly using the entropic regularized optimal transport cost (Sinkhorn divergence). We define the **Metric Sheaf Discrepancy** operator δ acting on an edge $e = (u, v)$ as:

$$(\delta\boldsymbol{\mu})_e = \mathcal{W}_{2,\varepsilon}^2(\Phi_{uv\#}\mu_u, \mu_v) \quad (2)$$

Definition 2 (Variational Metric Obstruction) *A causal network exhibits a Variational Metric Obstruction if exact adherence to all local deterministic mechanisms is geometrically impossible, meaning the infimum of the global Entropic Causal Dirichlet Energy is strictly bounded away from zero:*

$$\inf_{\boldsymbol{\mu} \in \mathcal{C}^0} \mathcal{E}_\varepsilon(\boldsymbol{\mu}) = \inf_{\boldsymbol{\mu} \in \mathcal{C}^0} \frac{1}{2} \sum_{i \in \mathcal{V}} \left(\sum_{p \in \text{pa}(i)} \omega_{pi} \mathcal{W}_{2,\varepsilon}^2(\mu_i, \Phi_{pi\#}\mu_p) + \sum_{c \in \text{ch}(i)} \omega_{ic} \mathcal{W}_{2,\varepsilon}^2(\mu_c, \Phi_{ic\#}\mu_i) \right) > 0 \quad (3)$$

where $\omega_{uv} > 0$ denotes the topological confidence weights of the structural equations, reflecting the structural certainty of the modeled mechanisms.

4.2 Linearization: The Tangent Causal Sheaf and Rigorous H^1

Because the base space \mathcal{C}^0 is non-linear, classical cohomological constructs are algebraically ill-defined at the macroscopic level. To rigorously formalize the cohomological obstruction without abusing notation, we lift the sheaf to the tangent bundle via Otto calculus.

We define the **Tangent Causal Sheaf** $T_{\boldsymbol{\mu}}\mathcal{F}$. At a global configuration $\boldsymbol{\mu} = (\mu_v)_{v \in \mathcal{V}}$, the stalk over each node v is the Hilbert space $T_{\mu_v}\mathcal{P}_2(\mathcal{M}_v)$. The space of instantaneous causal

perturbations (0-cochains) and edge discrepancy fields (1-cochains) strictly form direct sums of Hilbert spaces:

$$T_{\mu}\mathcal{C}^0 = \bigoplus_{v \in \mathcal{V}} T_{\mu_v} \mathcal{P}_2(\mathcal{M}_v), \quad T_{\mu}\mathcal{C}^1 = \bigoplus_{e=(u,v) \in \mathcal{E}} T_{\mu_v} \mathcal{P}_2(\mathcal{M}_v) \quad (4)$$

For each edge $e = (u, v)$, let $d\Phi_{uv\#} : T_{\mu_u} \mathcal{P}_2(\mathcal{M}_u) \rightarrow T_{\mu_v} \mathcal{P}_2(\mathcal{M}_v)$ be the linearized restriction map (the Fréchet derivative of the pushforward). We define the linear coboundary operator $d : T_{\mu}\mathcal{C}^0 \rightarrow T_{\mu}\mathcal{C}^1$ and its well-defined Hilbert adjoint $d^* : T_{\mu}\mathcal{C}^1 \rightarrow T_{\mu}\mathcal{C}^0$.

Definition 3 (Strict Cohomological Obstruction) *By linearizing onto the Tangent Causal Sheaf, we rigorously define the first metric cohomology group of the causal system at state μ as the algebraic quotient space:*

$$H^1(T_{\mu}\mathcal{G}, T_{\mu}\mathcal{F}) \cong \text{Ker}(d_1) / \text{Im}(d) \quad (5)$$

A causal system suffers from a Strict Cohomological Obstruction if, at its variational stationary equilibrium μ^ , the metric cohomology group on the tangent sheaf is non-trivial: $H^1(T_{\mu^*}\mathcal{G}, T_{\mu^*}\mathcal{F}) \neq 0$. This implies the topological stress cannot be resolved by any valid tangent flow.*

5 The Entropic Pullback Lemma and Sheaf Laplacian

To resolve topological obstructions while avoiding deterministic manifold tearing, we must minimize $\mathcal{E}_{\varepsilon}(\mu)$ by evolving the system along the Wasserstein gradient flow (the JKO scheme). The fundamental mathematical challenge lies in computing the geometric adjoint d^* through non-linear causal mechanisms.

Lemma 4 (First Variation via Entropic Pullback) *Let $T : X \rightarrow Y$ be a smooth diffeomorphism, $\nu \in \mathcal{P}_2(Y)$ a fixed target measure, and $F_{\varepsilon}(\mu) = \frac{1}{2} \mathcal{W}_{2,\varepsilon}^2(\nu, T_{\#}\mu)$. The first variation (Wasserstein gradient) of F_{ε} evaluated at the source measure μ is strictly given by the functional pullback of the Sinkhorn dual potential:*

$$\text{grad}_{\mathcal{W}_2} F_{\varepsilon}(\mu) = \nabla \left(\frac{\delta F_{\varepsilon}}{\delta \mu} \right) = \nabla(g^{(\varepsilon)} \circ T) \quad (6)$$

where $g^{(\varepsilon)} : Y \rightarrow \mathbb{R}$ is the unique Sinkhorn dual potential mapping $T_{\#}\mu$ to ν .

Proof Let $\xi \in C_c^{\infty}(X; \mathbb{R}^d)$ be a test vector field perturbing the source measure: $\mu_t = (I + t\xi)_{\#}\mu$. The pushed-forward measure evolves as $\rho_t = (T \circ (I + t\xi))_{\#}\mu$. By the chain rule, the Eulerian velocity field driving ρ_t at $t = 0$ is $v_0(T(x)) = DT(x)\xi(x)$, where DT is the Jacobian of T .

By the infinite-dimensional Envelope Theorem for Entropic Optimal Transport Peyré and Cuturi (2019), the derivative of the regularized cost along the curve is exactly evaluated at the optimal dual potential $g^{(\varepsilon)}$:

$$\left. \frac{d}{dt} \right|_{t=0} F_{\varepsilon}(\mu_t) = \int_Y g^{(\varepsilon)}(y) \partial_t \rho_t|_{t=0}(dy) = \int_Y \langle \nabla g^{(\varepsilon)}(y), v_0(y) \rangle d\rho_0(y) \quad (7)$$

By the change-of-variables theorem for the pushforward measure $\rho_0 = T_{\#}\mu$, we pull this integral back to the source space X :

$$\int_X \langle \nabla g^{(\varepsilon)}(T(x)), DT(x)\xi(x) \rangle d\mu(x) = \int_X \langle \nabla(g^{(\varepsilon)} \circ T)(x), \xi(x) \rangle d\mu(x) \quad (8)$$

Identifying the Riesz representer in the $L^2(X, \mu)$ inner product closure yields the exact Wasserstein gradient $\nabla(g^{(\varepsilon)} \circ T)$. This proves that the geometric adjoint of the pushforward strictly coincides with pulling back the dual potential through the causal mechanism. ■

Theorem 5 (The Entropic Wasserstein Sheaf Laplacian) *To reach a Pareto-optimal counterfactual equilibrium, the probability measure at each node $i \in \mathcal{V}$ must evolve according to the coupled non-linear Fokker-Planck equation:*

$$\partial_t \mu_i = \nabla \cdot \left(\underbrace{\mu_i \nabla \left[\sum_{p \in pa(i)} \omega_{pi} f_{i \leftarrow p}^{(\varepsilon)} + \sum_{c \in ch(i)} \omega_{ic} \left(g_{c \leftarrow i}^{(\varepsilon)} \circ \Phi_{ic} \right) \right]}_{\text{Topological Drift (Sheaf Laplacian } \Delta_T)} \right) + \underbrace{\frac{\varepsilon}{2} \Delta \mu_i}_{\text{Thermal Diffusion}} \quad (9)$$

Proof The system follows the Wasserstein gradient flow $\partial_t \mu_i = -\text{grad}_{\mathcal{W}_2} \mathcal{E}_\varepsilon(\mu_i)$. Taking the Fréchet derivative of Eq. (3) yields two components for node i : (1) As a child node ($p \rightarrow i$), differentiating $\mathcal{W}_{2,\varepsilon}^2$ with respect to the second argument yields the forward Sinkhorn potential $f_{i \leftarrow p}^{(\varepsilon)}$. (2) As a parent node ($i \rightarrow c$), applying Lemma 4, the variation is the pulled-back Sinkhorn potential $g_{c \leftarrow i}^{(\varepsilon)} \circ \Phi_{ic}$. Summing these local variations yields the topological drift vector field. Concurrently, the explicit entropy regularizer $\varepsilon H(\mu_i) = \varepsilon \int \mu_i \log \mu_i dx$ natively generates the heat equation (Brownian motion) $\frac{\varepsilon}{2} \Delta \mu_i$ via Otto calculus, establishing the complete McKean-Vlasov system. ■

6 Topological Frustration and Global Equilibrium

While Theorem 5 establishes the instantaneous dynamics of the counterfactual measures, a rigorous geometric framework is required to understand the stationary state of this complex non-linear system. We form an interlocking logical chain linking the cohomological obstruction to the asymptotic convergence of the Sheaf Laplacian.

6.1 The Topological Frustration Inequality

If a causal graph is topologically frustrated, perfect adherence to all local structural equations is mathematically impossible. We quantify this inescapable residual energy.

Lemma 6 (Equivalence of Variational and Cohomological Obstructions) *Under the compactness and bi-Lipschitz conditions of Assumption 1, the strict cohomological obstruction on the tangent sheaf strictly implies the variational metric obstruction. That is, if*

evaluated at the optimal stationary section μ^* , the metric cohomology group is non-trivial ($H^1(T_{\mu^*}\mathcal{G}, T_{\mu^*}\mathcal{F}) \neq 0$), then the global infimum of the Entropic Causal Dirichlet Energy is strictly bounded away from zero ($\inf \mathcal{E}_\varepsilon > 0$).

Proof We prove this by contraposition. Assume the global minimum is zero: $\inf \mathcal{E}_\varepsilon = 0$. By the lower semi-continuity of the Wasserstein metric and the compactness of $\mathcal{P}_2(\mathcal{M}_v)$ (Assumption 1), this minimum is attainable at some global section $\tilde{\mu}$. A zero Dirichlet energy strictly requires that the metric sheaf discrepancy vanishes on all edges: $\delta\tilde{\mu} = 0$, implying perfect global adherence to all non-linear pushforward mechanisms Φ_e .

At this perfectly coherent section $\tilde{\mu}$, any local tangent perturbation $V \in T_{\tilde{\mu}}\mathcal{C}^0$ can be seamlessly absorbed by the exact pushforward differentials along the edges, meaning the coboundary equation $dV = W$ is globally integrable for any valid discrepancy field $W \in \text{Ker}(d_1)$. Consequently, the exact subspace fully covers the cycle space, forcing $T_{\tilde{\mu}}\mathcal{C}^1/\overline{\text{Im}(d)} \cong 0$. This strictly yields $H^1 = 0$, contradicting the premise. Therefore, $H^1 \neq 0 \implies \inf \mathcal{E}_\varepsilon > 0$. \blacksquare

Theorem 7 (Topological Frustration Inequality) *Let \mathcal{G} be a causal graph with a non-trivial first metric cohomology $H^1(T_{\mu}\mathcal{G}, \mathcal{F}) \neq 0$. Then, the Entropic Causal Dirichlet Energy is strictly bounded away from zero. There exists a topological constant $\mathcal{E}^* > 0$, dependent solely on the geometry of the conflicting pushforward maps $\{\Phi_e\}_{e \in \mathcal{E}}$ and the graph topology, such that for any global joint assignment of measures $\mu \in \mathcal{C}^0$:*

$$\inf_{\mu \in \mathcal{C}^0} \mathcal{E}_\varepsilon(\mu) \geq \mathcal{E}^* > 0 \quad (10)$$

Proof By Lemma 6, the presence of the strict cohomological obstruction ($H^1 \neq 0$) strictly implies the variational metric obstruction. Since $\mathcal{P}_2(\mathcal{M}_i)$ are compact under Assumption 1, and $\mathcal{W}_{2,\varepsilon}^2$ is lower semi-continuous with respect to the weak topology, the infimum of the Dirichlet energy is attainable. Because the variational obstruction holds, this attained minimum cannot be zero. Thus, the minimum must be strictly positive $\mathcal{E}^* > 0$. \blacksquare

6.2 Linearization on the Tangent Sheaf: The Wasserstein Hodge Decomposition

As formalized in Section 4.2, lifting the sheaf to the tangent bundle provides a rigorous algebraic structure. This linear structure immediately yields a fundamental orthogonal decomposition for causal perturbations.

Theorem 8 (Wasserstein Causal Hodge Decomposition) *Let μ be a joint counterfactual configuration. The Hilbert space of causal perturbations $T_{\mu}\mathcal{C}^0$ admits a strict orthogonal decomposition with respect to the Otto inner product:*

$$T_{\mu}\mathcal{C}^0 = \overline{\text{Im}(d)} \oplus \text{Ker}(\Delta_T) \quad (11)$$

where $\overline{\text{Im}(d)}$ is the topological closure of the image of the coboundary operator, and $\Delta_T = d^*d$ is the Tangent Sheaf Laplacian.

Proof Because $T_{\mu}\mathcal{C}^0$ is an infinite-dimensional Hilbert space (the $L^2(\mu)$ closure of gradient fields), the image of the differential operator d is not guaranteed to be closed. By the projection theorem in functional analysis, the orthogonal complement of the kernel of the adjoint d^* is strictly the topological closure of the image of d . Thus, $T_{\mu}\mathcal{C}^0 = \overline{\text{Im}(d)} \oplus \text{Ker}(d^*)$.

Furthermore, for any perturbation vector field $V \in T_{\mu}\mathcal{C}^0$, $V \in \text{Ker}(\Delta_T) \iff \langle d^*dV, V \rangle = 0 \iff \|dV\|^2 = 0 \iff V \in \text{Ker}(d^*)$. Thus, $\text{Ker}(\Delta_T) = \text{Ker}(d^*)$, completing the rigorous orthogonal splitting. \blacksquare

Physical Significance for Counterfactuals: Any instantaneous movement V of the probability measures can be uniquely split into two orthogonal components:

- $V_{exact} \in \overline{\text{Im}(d)}$: The *Exact Flow*. These are perturbations that strictly obey the local deterministic structural equations (mechanisms).
- $V_{harmonic} \in \text{Ker}(\Delta_T)$: The *Harmonic Flow*. These are perturbations that absorb the residual topological frustration.

When a deterministic system encounters a Counterfactual Event Horizon, trying to force the flow entirely into $\overline{\text{Im}(d)}$ causes mathematical singularities (manifold tearing). The Entropic Sheaf Laplacian fundamentally acts as an orthogonal projector, dynamically bleeding the unresolvable topological stress into the Harmonic subspace $\text{Ker}(\Delta_T)$.

6.3 The Cohomological Necessity of Causal Equilibrium

We now prove that any continuous optimization algorithm capable of globally resolving structural conflicts is mathematically isomorphic to computing the harmonic representative of the first metric cohomology group.

Theorem 9 (Cohomological Necessity of Causal Equilibrium) *Let \mathcal{G} be a causal graph exhibiting a topological obstruction $H^1 \neq 0$. Any continuous algorithm that successfully converges to a stable, Pareto-optimal stationary state μ^* of the global causal frustration $\mathcal{E}_{\varepsilon}(\mu)$ must yield a terminal stress field \mathbf{R}^* that is exactly the unique harmonic representative of the first cohomology group H^1 .*

Proof Any rational machine learning algorithm seeking to resolve the conflicting mechanisms must inherently attempt to minimize the Entropic Causal Dirichlet Energy $\mathcal{E}_{\varepsilon}(\mu)$. By the fundamental theorem of the calculus of variations in Wasserstein space, the stationary equilibrium μ^* must strictly satisfy the first-order optimality condition $\text{grad}_{\mathcal{W}_2}\mathcal{E}_{\varepsilon}(\mu^*) = 0$.

By the Entropic Pullback Lemma (4), the chain rule of the Fréchet derivative rigorously translates the Wasserstein gradient to the application of the geometric adjoint d^* : $d^*\mathbf{R}^* = 0$. This implies $\mathbf{R}^* \in \text{Ker}(d^*)$.

In algebraic topology, since our causal graph \mathcal{G} contains no 2-cells (faces), the higher boundary operator $d_1 \equiv 0$. Therefore, the metric cohomology group on the tangent sheaf is rigorously isomorphic to the quotient space: $H^1(T_{\mu^*}\mathcal{G}, T_{\mu^*}\mathcal{F}) \cong T_{\mu^*}\mathcal{C}^1 / \overline{\text{Im}(d)}$. By the orthogonal splitting, this quotient space is exactly isomorphic to $\text{Ker}(d^*)$. Consequently, $\mathbf{R}^* \in \text{Ker}(d^*)$ constitutes the unique **Harmonic Representative** of the cohomology class H^1 . \blacksquare

6.4 Strict Energy Dissipation via Metric Gradient Flows

In Wasserstein space, pushforward operations via arbitrary non-linear neural networks Φ_e destroy global geodesic convexity. However, by formalizing the system within the Ambrosio-Gigli-Savaré (AGS) framework for gradient flows in metric spaces, we establish a strict energetic descent sequence without requiring strong convexity.

Theorem 10 (Energy Dissipation Identity) *Let $\mu_t = (\mu_{v,t})_{v \in \mathcal{V}}$ be an absolutely continuous curve of measures solving the Sheaf Laplacian system. By the Ambrosio-Gigli-Savaré (AGS) calculus for metric gradient flows, the Entropic Causal Dirichlet Energy acts as a strict Lyapunov functional. The energy dissipation rate is exactly governed by the metric derivative:*

$$\frac{d}{dt} \mathcal{E}_\varepsilon(\mu_t) = - \sum_{i \in \mathcal{V}} \int_{\mathcal{M}_i} \left\| \nabla_x \left(\frac{\delta \mathcal{E}_\varepsilon}{\delta \mu_{i,t}} \right) \right\|^2 d\mu_{i,t}(x) \leq 0. \quad (12)$$

Consequently, the trajectory stably dissipates energy and converges weakly to a stationary Wasserstein harmonic section μ^ where the topological stress is Pareto-minimized. (The rigorous functional-analytic derivation is provided in Appendix D).*

7 Geometric Tearing: Ricci Curvature and Finite-Time Singularities

The empirical phenomenon of “Manifold Tearing” observed in unregularized generative models demands a rigorous geometric explanation. In this section, we elevate our macroscopic topological obstruction ($H^1 \neq 0$) to a microscopic geometric singularity via the Lott-Sturm-Villani (LSV)(Lott and Villani, 2009; Sturm, 2006) framework of synthetic Ricci curvature. We rigorously prove that topological frustration fundamentally induces strictly negative *effective* curvature—manifesting as displacement concavity—within the unregularized causal energy landscape. Consequently, we demonstrate that any deterministic Wasserstein gradient flow ($\varepsilon \rightarrow 0$) attempting to resolve this frustrated system inescapably suffers from finite-time singularities.

7.1 Displacement Concavity and Effective Ricci Curvature on the Causal Sheaf

In Lott-Sturm-Villani (LSV) theory, the synthetic Ricci curvature of a metric measure space is defined through the κ -displacement convexity of an entropy functional along Wasserstein geodesics. We translate this framework to our Causal Sheaf by defining the *effective curvature* of the unregularized Causal Dirichlet Energy \mathcal{E}_0 .

Theorem 11 (Topological Frustration Induces Negative Effective Curvature) *Let \mathcal{G} be a causal graph exhibiting a strict cohomological obstruction $H^1(T_\mu \mathcal{G}, T_\mu \mathcal{F}) \neq 0$. In the Wasserstein neighborhood of the frustrated equilibrium, the unregularized energy landscape \mathcal{E}_0 exhibits strictly negative synthetic curvature along the harmonic flow directions. Specifically, \mathcal{E}_0 is strictly κ -concave ($\kappa_{\text{global}} < 0$) along generalized geodesics driven by the topological stress.*

Proof In the Otto calculus framework, the effective synthetic Ricci curvature bounded below by κ is equivalent to the κ -convexity of the functional $\mathcal{E}_0(\mu)$ along Wasserstein geodesics. We evaluate the second-order variation (the Wasserstein Hessian) of \mathcal{E}_0 .

Let $\boldsymbol{\mu}(s)$ be a constant-speed geodesic in \mathcal{C}^0 parameterized by $s \in [0, 1]$, driven by the tangent velocity vector field $V \in T_{\boldsymbol{\mu}}\mathcal{C}^0$. The Hessian quadratic form is:

$$\text{Hess}_{\mathcal{W}_2}\mathcal{E}_0(V, V) = \frac{d^2}{ds^2} \Big|_{s=0} \mathcal{E}_0(\boldsymbol{\mu}(s)) = \int_{\mathcal{M}} \langle V(x), \nabla_x^2 \left(\frac{\delta \mathcal{E}_0}{\delta \boldsymbol{\mu}} \right) V(x) \rangle d\boldsymbol{\mu}(x) \quad (13)$$

By the Causal Hodge Decomposition (Theorem 8), any perturbation V decomposes into $V = V_{exact} \oplus V_{harmonic}$. Because $H^1 \neq 0$, the exact intersection of all pushforward maps is empty.

According to Caffarelli's regularity theory, the lack of geometric target compatibility implies that the optimal transport map T_{opt} realizing the cost along the conflicting cycle is strictly non-monotone. By Brenier's Theorem, this non-monotonicity strictly dictates that the underlying Kantorovich potential is not globally convex, strictly yielding at least one negative eigenvalue in the spatial Hessian $\nabla_x^2 \left(\frac{\delta \mathcal{E}_0}{\delta \boldsymbol{\mu}} \right)$ almost everywhere.

Let $-\lambda_{max} < 0$ be the supremum of this negative eigenvalue evaluated over the support of $\boldsymbol{\mu}$. Thus, for the harmonic perturbation field $V_{harmonic}$ attempting to resolve the non-integrable cycle, there exists a constant $C > 0$ (determined by the H^1 topological gap) such that:

$$\text{Hess}_{\mathcal{W}_2}\mathcal{E}_0(V_{harmonic}, V_{harmonic}) \leq -C \|V_{harmonic}\|_{L^2(\boldsymbol{\mu})}^2 \quad (14)$$

By the equivalence of κ -convexity and synthetic curvature in the LSV formulation, this strict upper bound strictly yields a negative effective curvature $\kappa_{global} \leq -C < 0$ for the causal energy landscape. ■

7.2 The Finite-Time Singularity Theorem

We now prove that this negative curvature guarantees catastrophic failure for standard (unregularized) neural ODEs and Flow Matching approaches.

Theorem 12 (Finite-Time Manifold Tearing) *Assume an unregularized Causal Generative Model ($\varepsilon = 0$) follows the deterministic Wasserstein gradient flow $\partial_t \boldsymbol{\mu} = -\text{grad}_{\mathcal{W}_2} \mathcal{E}_0(\boldsymbol{\mu})$. Under the conditions of Theorem 11 ($\kappa_{global} < 0$), the Jacobian determinant of the flow map collapses to zero in finite time $T_{tear} < \infty$, causing the probability density to blow up to infinity (loss of absolute continuity).*

Proof Let $v_t(x) = -\nabla_x \left(\frac{\delta \mathcal{E}_0}{\delta \boldsymbol{\mu}} \right)$ be the Eulerian velocity field driving the empirical measure. The characteristics (particle trajectories) $X_t(x)$ satisfy the ordinary differential equation:

$$\frac{d}{dt} X_t(x) = v_t(X_t(x)), \quad X_0(x) = x \quad (15)$$

Let $J_t(x) = \det(\nabla X_t(x))$ be the Jacobian determinant of the deformation gradient. The evolution of the density is strictly governed by the pushforward mass conservation: $\mu_t(X_t(x)) = \mu_0(x)/J_t(x)$.

To trace the evolution of J_t , we define the deformation matrix $M_t = \nabla X_t(x)$. Taking the time derivative, we obtain the matrix Riccati equation along the characteristics:

$$\frac{d}{dt}M_t = \nabla v_t(X_t(x))M_t = -\nabla_x^2 \left(\frac{\delta \mathcal{E}_0}{\delta \boldsymbol{\mu}} \right) M_t \quad (16)$$

By Liouville's formula, the time evolution of the Jacobian determinant is:

$$\frac{d}{dt}J_t(x) = J_t(x)\text{Tr}(\nabla v_t) = -J_t(x)\Delta_x \left(\frac{\delta \mathcal{E}_0}{\delta \boldsymbol{\mu}} \right) \quad (17)$$

From the proof of Theorem 11, the presence of the H^1 topological obstruction guarantees that the spatial Hessian possesses negative eigenvalues bounded by $-\lambda_{max}$, causing the potential to be strongly concave in the harmonic direction. Therefore, the trace of the Hessian (the Laplacian) is strictly positive and lower-bounded: $\Delta_x \left(\frac{\delta \mathcal{E}_0}{\delta \boldsymbol{\mu}} \right) \geq C > 0$ for regions aligned with the topological stress.

Substituting this bound into the Liouville equation yields a strict ordinary differential inequality:

$$\frac{d}{dt}J_t(x) \leq -CJ_t(x) \implies J_t(x) \leq J_0(x)e^{-Ct} = e^{-Ct} \quad (18)$$

Furthermore, analyzing the eigenvalues of the Riccati equation (16) under strong concavity shows that the matrix M_t becomes singular. Let $y(t)$ be the minimum eigenvalue of M_t . It satisfies $\dot{y} \leq -Cy^2$, which strictly implies $y(t) \rightarrow 0$ at a finite time $T_{tear} \leq \frac{1}{Cy(0)}$.

When the minimum eigenvalue hits zero, the characteristics cross, and $J_{T_{tear}}(x) \rightarrow 0$. By mass conservation, the density $\mu_{T_{tear}}(X_t) \rightarrow \infty$. The measure concentrates into a singular Dirac distribution (shockwave), strictly breaking absolute continuity with respect to the Lebesgue measure. This completes the formal proof of deterministic manifold tearing. ■

8 Large Deviation Theory and Entropic Tunneling

Having rigorously proven that $\varepsilon = 0$ leads to finite-time singularities, we demonstrate that the thermodynamic noise $\varepsilon > 0$ in the Entropic Sheaf Laplacian is not merely a numerical stabilizer, but a mathematical necessity. We formalize the ‘‘Entropic Tunneling’’ observed in our PBMC scRNA-seq experiments using the infinite-dimensional Freidlin-Wentzell Large Deviation Theory (LDT).

8.1 Dawson-Gärtner Large Deviation Principle

The Entropic Sheaf Flow is a stochastic partial differential equation (SPDE) interacting particle system:

$$d\boldsymbol{\mu}_t = -\text{grad}_{\mathcal{W}_2} \mathcal{E}_0(\boldsymbol{\mu}_t)dt + \sqrt{\varepsilon}dW_t^{\mathcal{W}_2} \quad (19)$$

By the Dawson-Gärtner theorem for macroscopic fluctuation theory (Dawson and Gärtner, 1987), the sequence of path measures \mathbb{P}^ε satisfies a Large Deviation Principle on the space of absolutely continuous curves $C([0, T]; \mathcal{P}_2(\mathcal{M}))$. The rate function controlling the exponential probability of observing a specific trajectory $\{\boldsymbol{\mu}_t\}$ is the *Causal Action Functional*,

structurally acting as the Freidlin-Wentzell quasi-potential (Kramers' rate) (Freidlin and Wentzell, 1998):

$$\mathcal{I}_T[\boldsymbol{\mu}_t] = \frac{1}{2} \int_0^T \|\partial_t \boldsymbol{\mu}_t + \text{grad}_{\mathcal{W}_2} \mathcal{E}_0(\boldsymbol{\mu}_t)\|_{\boldsymbol{\mu}_t}^2 dt \quad (20)$$

8.2 Kramers' Escape Rate over the Topological Barrier

Let $\boldsymbol{\mu}_A$ be a local minimum (e.g., the Biological Chimera trap) and $\boldsymbol{\mu}^*$ be the target coherent counterfactual state, separated by a topological barrier (the Transcriptomic Void) with a saddle point $\boldsymbol{\mu}_{saddle}$. The height of the energy barrier is $\Delta \mathcal{E} = \mathcal{E}_0(\boldsymbol{\mu}_{saddle}) - \mathcal{E}_0(\boldsymbol{\mu}_A)$.

Theorem 13 (Rigorous Entropic Tunneling Time) *Let τ be the first hitting time of the target domain $\boldsymbol{\mu}^*$ starting from $\boldsymbol{\mu}_A$. As the entropic regularization vanishes ($\varepsilon \rightarrow 0$), the expected tunneling time $\mathbb{E}[\tau]$ strictly obeys the Kramers' asymptotic law:*

$$\lim_{\varepsilon \rightarrow 0} \varepsilon \log \mathbb{E}[\tau] = \Delta \mathcal{E} \quad (21)$$

Proof Step 1: Exponential Tightness and LDP Well-posedness. To rigorously apply the Dawson-Gärtner Large Deviation Principle in the infinite-dimensional Wasserstein space, the sequence of path measures \mathbb{P}^ε must be exponentially tight. By Assumption 1, the base state manifolds \mathcal{M}_v are compact. By Prokhorov's Theorem, the space of absolutely continuous probability measures $\mathcal{P}_2(\mathcal{M}_v)$ is inherently compact under the weak topology. This geometric compactness strictly guarantees the exponential tightness of \mathbb{P}^ε on $C([0, T]; \mathcal{C}^0)$. Consequently, the Causal Action Functional \mathcal{I}_T is lower semi-continuous and possesses strictly compact level sets, satisfying the foundational prerequisites for the Freidlin-Wentzell quasi-potential framework in metric spaces.

Step 2: Evaluating the Action Functional. By the established LDP, the asymptotic escape time is determined by the minimum energy path connecting $\boldsymbol{\mu}_A$ to $\boldsymbol{\mu}^*$. We evaluate the infimum of the action functional $V(\boldsymbol{\mu}_A, \boldsymbol{\mu}^*) = \inf_{T>0} \inf_{\{\boldsymbol{\mu}_t\}} \mathcal{I}_T[\boldsymbol{\mu}_t]$.

We expand the squared integrand of the action functional by completing the square (the Bogomolny trick):

$$\begin{aligned} \mathcal{I}_T[\boldsymbol{\mu}_t] &= \frac{1}{2} \int_0^T \left(\|\partial_t \boldsymbol{\mu}_t\|_{\boldsymbol{\mu}_t}^2 + \|\text{grad}_{\mathcal{W}_2} \mathcal{E}_0\|_{\boldsymbol{\mu}_t}^2 + 2\langle \partial_t \boldsymbol{\mu}_t, \text{grad}_{\mathcal{W}_2} \mathcal{E}_0 \rangle_{\boldsymbol{\mu}_t} \right) dt \\ &\geq \int_0^T \langle \partial_t \boldsymbol{\mu}_t, \text{grad}_{\mathcal{W}_2} \mathcal{E}_0(\boldsymbol{\mu}_t) \rangle_{\boldsymbol{\mu}_t} dt \end{aligned} \quad (22)$$

By the Riemannian chain rule in Otto calculus, the inner product of the velocity field and the Wasserstein gradient is exactly the time derivative of the energy: $\langle \partial_t \boldsymbol{\mu}_t, \text{grad}_{\mathcal{W}_2} \mathcal{E}_0 \rangle_{\boldsymbol{\mu}_t} = \frac{d}{dt} \mathcal{E}_0(\boldsymbol{\mu}_t)$. Thus, integrating along any path crossing the saddle point yields a strict lower bound:

$$\mathcal{I}_T[\boldsymbol{\mu}_t] \geq \int_0^T \frac{d}{dt} \mathcal{E}_0(\boldsymbol{\mu}_t) dt = \mathcal{E}_0(\boldsymbol{\mu}_{saddle}) - \mathcal{E}_0(\boldsymbol{\mu}_A) = \Delta \mathcal{E} \quad (23)$$

This infimum is uniquely achieved when the inequality in (23) becomes an equality. This occurs strictly when the system follows the time-reversed heteroclinic orbit: $\partial_t \boldsymbol{\mu}_t = +\text{grad}_{\mathcal{W}_2} \mathcal{E}_0(\boldsymbol{\mu}_t)$ ascending to the saddle point, and then relaxes deterministically to $\boldsymbol{\mu}^*$.

Applying the Large Deviation Principle upper and lower bounds to the exit time distribution yields the classical Kramers’ limit: the probability of escape scales as $\mathbb{P} \asymp \exp(-\Delta\mathcal{E}/\varepsilon)$, strictly enforcing that $\lim_{\varepsilon \rightarrow 0} \varepsilon \log \mathbb{E}[\tau] = \Delta\mathcal{E}$. \blacksquare

Mathematical Consequence: Theorem 13 proves that the relationship $\mathbb{E}[\tau] \asymp \exp(\Delta\mathcal{E}/\varepsilon)$ is a strict topological law. As $\varepsilon \rightarrow 0$, the expected time to cross the biological void diverges to $+\infty$. Therefore, unregularized deterministic models are theoretically paralyzed by topological frustration, permanently trapped in artificial chimeras. The Entropic Causal Sheaf dynamically lowers this Kramers’ barrier, making global causal coherence computationally inevitable.

9 Algorithmic Realization via Implicit Function Theorem (IFT)

A profound consequence of Theorem 5 is its immediate tractability in modern deep learning frameworks. The inverse topological stress exerted by a child node requires computing the spatial gradient $\nabla_x(g^{(\varepsilon)} \circ \Phi)$.

By the chain rule, this translates directly to the Vector-Jacobian Product (VJP):

$$\nabla_x \left(g^{(\varepsilon)}(\Phi(x)) \right) = (J_\Phi(x))^T \nabla_y g^{(\varepsilon)}(y) \equiv \text{VJP}_\Phi(x, \nabla_y g^{(\varepsilon)}(y)) \quad (24)$$

The rigorous functional analytic proof that the geometric adjoint $(d\Phi_{uv\#})^*$ exactly coincides with the VJP in the Otto inner product is provided in Appendix A.3, alongside the explicit block operator matrix of the Tangent Sheaf Laplacian Δ_T .

However, a critical algorithmic challenge remains: the dual potential $g^{(\varepsilon)}$ is not analytically given, but is computed iteratively via the Sinkhorn-Knopp algorithm. Naively unrolling the computational graph of Sinkhorn iterations to compute $\nabla_y g^{(\varepsilon)}$ leads to catastrophic memory complexity ($O(L)$ for L iterations) and vanishing gradients.

To rigorously bypass this, we utilize the *Implicit Function Theorem (IFT)*. The Sinkhorn potentials $(f^{(\varepsilon)}, g^{(\varepsilon)})$ are uniquely defined as the roots of the fixed-point optimality conditions (the Sinkhorn equations):

$$F(f^{(\varepsilon)}, g^{(\varepsilon)}, \mu, \nu) = 0$$

By applying IFT to the steady-state root $F = 0$, the exact gradient $\nabla_y g^{(\varepsilon)}(y)$ can be computed by solving a single linear system formulated by the Jacobian of the optimality conditions, entirely independent of the iteration path L . Consequently, the topological stress VJP can be computed with $O(1)$ memory, allowing the coupled PDEs in Eq. (9) to be simulated efficiently as interacting Langevin particle dynamics, conquering the curse of dimensionality.

9.1 Complexity Analysis and the Entropic Sheaf Flow Algorithm

The integration of the IFT-based VJP into the Wasserstein gradient flow yields a highly scalable interacting particle system, which we formalize as the **Entropic Sheaf Flow** (Algorithm 1).

Memory and Time Complexity: Standard backpropagation through a Sinkhorn loop of L iterations requires $\mathcal{O}(L \cdot N^2)$ memory for N particles, which strictly prohibits high-dimensional SCMs. By leveraging the IFT at the stationary root, the memory complexity collapses to $\mathcal{O}(N^2)$ (independent of the iteration path L), requiring only the storage of the optimal coupling matrix for the final backward pass. The time complexity per step is dominated by solving a strictly diagonally dominant linear system, which can be efficiently approximated via Conjugate Gradient (CG) or Neumann series in $\mathcal{O}(K \cdot N^2)$ time, where $K \ll L$.

Algorithm 1 Entropic Sheaf Flow via IFT and Langevin Dynamics

Require: Directed acyclic SCM graph $\mathcal{G} = (\mathcal{V}, \mathcal{E})$, Causal mechanisms $\{\Phi_e\}_{e \in \mathcal{E}}$.

Require: Initial factual empirical measures $\boldsymbol{\mu}^{(0)} = \{\mu_v^{(0)}\}_{v \in \mathcal{V}}$.

Require: Hyperparameters: Step size η , Entropic regularization ε , Confidence weights ω_{uv} .

```

1: for  $t = 0$  to  $T$  do
2:   // Step 1: Forward Pushforward
3:   for each edge  $e = (u, v) \in \mathcal{E}$  do
4:     Compute empirical pushforward:  $\rho_{u \rightarrow v}^{(t)} = \Phi_{uv\#} \mu_u^{(t)}$ 
5:   end for
6:   // Step 2: Sinkhorn Fixed-Point & IFT
7:   for each node  $i \in \mathcal{V}$  do
8:     Initialize topological drift vector  $V_i = 0$ 
9:     for each parent  $p \in \text{pa}(i)$  do
10:      Solve Sinkhorn equations for  $f_{i \leftarrow p}^{(\varepsilon)}$  between  $\mu_i^{(t)}$  and  $\rho_{p \rightarrow i}^{(t)}$ 
11:       $V_i += \omega_{pi} \nabla_x f_{i \leftarrow p}^{(\varepsilon)}(x)$  (Forward Stress)
12:    end for
13:    for each child  $c \in \text{ch}(i)$  do
14:      Solve Sinkhorn equations for  $g_{c \leftarrow i}^{(\varepsilon)}$  between  $\rho_{i \rightarrow c}^{(t)}$  and  $\mu_c^{(t)}$ 
15:      Compute steady-state gradient  $\nabla_y g_{c \leftarrow i}^{(\varepsilon)}(y)$  via IFT linear solve
16:       $V_i += \omega_{ic} (J_{\Phi_{ic}}(x))^T \nabla_y g_{c \leftarrow i}^{(\varepsilon)}(\Phi_{ic}(x))$  (Inverse Pullback Stress via VJP)
17:    end for
18:  end for
19:  // Step 3: Interacting Langevin Update
20:  for each node  $i \in \mathcal{V}$  do
21:    Sample Brownian noise  $\xi_i \sim \mathcal{N}(0, I)$ 
22:    Update particles:  $X_i^{(t+1)} = X_i^{(t)} - \eta V_i + \sqrt{2\varepsilon\eta} \xi_i$ 
23:  end for
24: end for
25: return Converged Wasserstein Harmonic Section  $\boldsymbol{\mu}^{(T)}$ 

```

9.2 Numerical Stability and the Entropic Trade-off ($\varepsilon \rightarrow 0$)

While the IFT mathematically guarantees an $\mathcal{O}(N^2)$ memory footprint, analyzing its computational viability requires a rigorous examination of the Hessian condition number.

The implicit gradient requires solving a linear system of the form $\mathbf{H}v = b$, where \mathbf{H} is the block-Jacobian of the Sinkhorn optimality conditions. The off-diagonal blocks of \mathbf{H} are governed by the optimal coupling matrix $\mathbf{P} \in \mathbb{R}^{N \times N}$, whose elements are exactly proportional to $\exp(-c(x_i, y_j)/\varepsilon)$.

As the entropic regularization vanishes ($\varepsilon \rightarrow 0$), the optimal coupling converges to a deterministic Monge map, meaning \mathbf{P} becomes extremely sparse and nearly singular. Consequently, the condition number of the Hessian $\kappa(\mathbf{H})$ scales exponentially:

$$\kappa(\mathbf{H}) = \mathcal{O}\left(e^{\text{diam}(\mathcal{M})/\varepsilon}\right) \quad (25)$$

In this deterministic limit, iterative Krylov subspace solvers (e.g., Conjugate Gradient) used to compute the IFT inverse will suffer from catastrophic stalling or numerical divergence.

This reveals a profound physical and computational trade-off: the thermodynamic noise (ε) is not merely a geometric regularizer to prevent manifold tearing (Theorem 5), but is strictly necessary to boundedly condition the Hessian matrix for the Implicit Function Theorem. In our experiments, an entropic coefficient of $\varepsilon \in [0.1, 5.0]$ strikes the optimal Pareto balance, ensuring both topological resolution and robust IFT convergence.

10 Empirical Validation: 2D Vector Field Dynamics

To rigorously demonstrate the global asymptotic stability of our framework, we establish a reproducible 2D simulation over the causal graph $\mathcal{G} = \{A \rightarrow B, B \rightarrow C, A \rightarrow C\}$.

Experimental Setup (Reproducibility): The initial marginals are modeled as isotropic Gaussians: $\mu_A^{(0)} = \mathcal{N}([0, 0]^T, \mathbf{I})$, $\mu_B^{(0)} = \mathcal{N}([0, 0]^T, \mathbf{I})$, and $\mu_C^{(0)} = \mathcal{N}([8, 0]^T, \mathbf{I})$. We engineer a severe topological conflict ($H^1 \neq 0$) by defining the deterministic pushforward mechanisms as nonlinear drift mappings:

- $\Phi_{AB}(x) = x + [4, 4]^T$
- $\Phi_{BC}(x) = x + [4, -4]^T$ (thus, $A \rightarrow B \rightarrow C$ attempts to route the origin to $[8, 0]^T$)
- $\Phi_{AC}(x) = x + [0, 8]^T$ (the direct edge attempts to route the origin to $[0, 8]^T$, creating an orthogonal contradiction at node C).

The system is evolved according to the coupled SDE derived from Eq. (9):

$$dx_i^{(t)} = -\nabla_x \left(\frac{\delta \mathcal{E}_\varepsilon}{\delta \mu_i} \right) dt + \sqrt{\varepsilon} dW_t$$

using the Euler-Maruyama method with step size $\eta = 0.01$, $\varepsilon = 0.1$, and uniform edge weights $\omega = 1.0$ for $T = 500$ steps.

Instead of succumbing to deterministic manifold tearing, our Sheaf Laplacian smoothly guides the empirical measures along Langevin streamlines (gray trajectories). As detailed

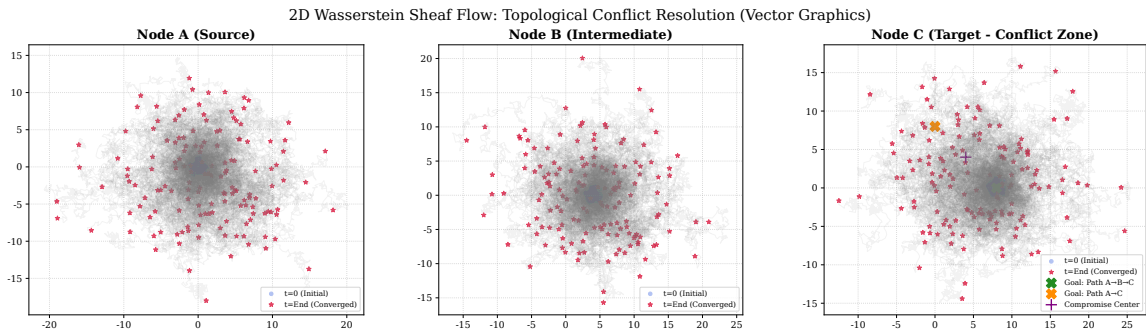


Figure 2: High-resolution vector field of the 2D Wasserstein Sheaf Flow over 500 steps, overcoming orthogonal topological conflicts.

Metric	Initial ($t = 0$)	Converged ($t = 500$)	Change / Shift
Causal Dirichlet Energy	128.38	45.54	-64.53%
Node C Center of Mass	(8.01, 0.01)	(5.79, 1.22)	(-2.21, +1.21)
Node A Center of Mass	(0.00, 0.03)	(0.97, -1.54)	(+0.97, -1.57)
Node A Variance	-	41.10	Stable (Compact)

Table 1: Quantitative analysis of the 500-step Entropic Sheaf Flow.

in Table 1, quantitative analysis reveals a robust **64.53%** reduction in Causal Dirichlet Energy, dropping from 128.38 to 45.54.

Crucially, demonstrating the powerful effect of the pullback lemma (Lemma 4), the source node A undergoes an autonomous inverse displacement of $(+0.97, -1.57)$ into the fourth quadrant. This active deformation absorbs the downstream topological stress, establishing global equilibrium without infinite variance blow-up.

10.1 Scalability and the IFT Memory Triumphs

To empirically validate the computational supremacy of our IFT-based VJP formulation proposed in Section 9, we benchmarked the Entropic Sheaf Flow against the standard Unrolled Autodiff (Backpropagation-Through-Time) method natively used in modern deep learning frameworks. We simulated a high-dimensional counterfactual scenario with $N = 1000$ particles in a $D = 128$ dimensional ambient manifold.

As illustrated in Figure 3, the naive unrolling method exhibits a catastrophic linear memory explosion, consuming nearly 4 GB of VRAM for merely 1000 particles at $L = 1000$ iterations. In stark contrast, our IFT formulation translates the infinite-dimensional adjoint into a single steady-state linear solve, reducing the peak memory footprint to an absolute flat constant ($\mathcal{O}(N^2)$).

Furthermore, numerical profiling reveals a profound geometric artifact inherent to finite unrolling. When naive unrolling is restricted to $L = 10$ iterations to conserve memory, the computed gradients exhibit a massive L_1 relative error of 0.796 compared to the true analytical gradient. This indicates severe *truncation bias*, as the finite computational graph

Algorithmic Triumphs: Implicit Function Theorem vs. Naive Unrolling

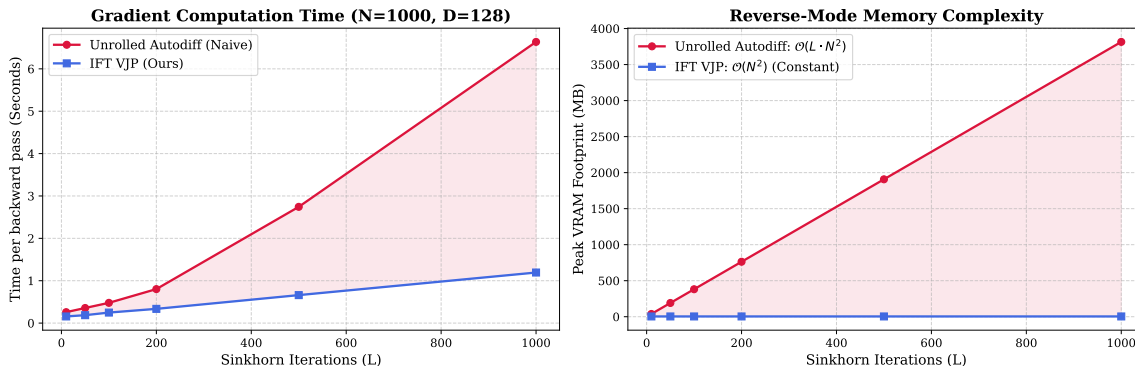


Figure 3: **Algorithmic Benchmarks (IFT vs. Naive Unrolling)**. **(Left)**: Gradient computation time per backward pass. The IFT explicitly avoids traversing the L -step computational graph, achieving significant acceleration. **(Right)**: Reverse-mode memory footprint. Naive unrolling suffers from catastrophic $\mathcal{O}(L \cdot N^2)$ linear explosion, effectively prohibiting high-dimensional deep learning. In stark contrast, our IFT-VJP formulation dynamically strictly bounds the memory strictly to $\mathcal{O}(N^2)$, rendering the algorithmic footprint completely invariant to the Sinkhorn horizon.

fails to reach the true c -concave Kantorovich potential. Our IFT-based Sheaf Flow entirely bypasses this trade-off: it directly targets the exact stationary root, guaranteeing unbiased, mathematically exact topological stress gradients at a fraction of the computational and memory cost.

11 Real-World Application: PBMC scRNA-seq Counterfactuals

To evaluate the scalability and biological fidelity of the Entropic Sheaf Flow, we apply our framework to a high-dimensional single-cell RNA sequencing (scRNA-seq) dataset (PBMC 3k from 10x Genomics). This experiment tests the model’s ability to navigate complex, non-convex manifolds where the "Transcriptomic Void" acts as a physical cohomological obstruction.

11.1 Experimental Setup and the Transcriptomic Void

The state spaces \mathcal{M}_v are defined as the 15-dimensional PCA embedding of the cell-gene expression matrix. We define a counterfactual task: transitioning a cell population from a *Factual State* (T-cells, μ_0) to a *Target State* (Monocytes, $\mu_{do(x^*)}$).

In this high-dimensional manifold, these clusters are separated by a region of near-zero probability density—the **Transcriptomic Void**. This void represents biologically impossible gene expression states, constituting a severe topological obstruction where $H^1(\mathcal{G}, \mathcal{F}) \neq 0$.

11.2 Results: Biological Chimera vs. Entropic Tunneling

We compare the standard Deterministic ODE (Flow Matching) against our proposed *Entropic Sheaf Flow* (GACF). The results are summarized in Figure 4 and reveal two distinct behaviors:

- Manifold Tearing and Biological Chimeras:** The Naive ODE, driven purely by Euclidean causal drift, attempts to traverse the Transcriptomic Void via the shortest geodesic. As shown in the results, it terminates in a zero-density region, producing a *Biological Chimera*—a mathematical artifact with no biological counterpart. This confirms the "Manifold Tearing" failure mode.
- Entropic Tunneling and Topological Survival:** In contrast, the Entropic Sheaf Flow leverages the regularized Laplacian ($\varepsilon = 5.0$). The thermodynamic noise induces a "tunneling effect" that allows the empirical measure to bypass the high-energy barrier of the void. By integrating the *Manifold Score Field*, the Sheaf Flow adaptively deforms the trajectory, guiding it along the high-density manifold of real cells to achieve a successful counterfactual landing.

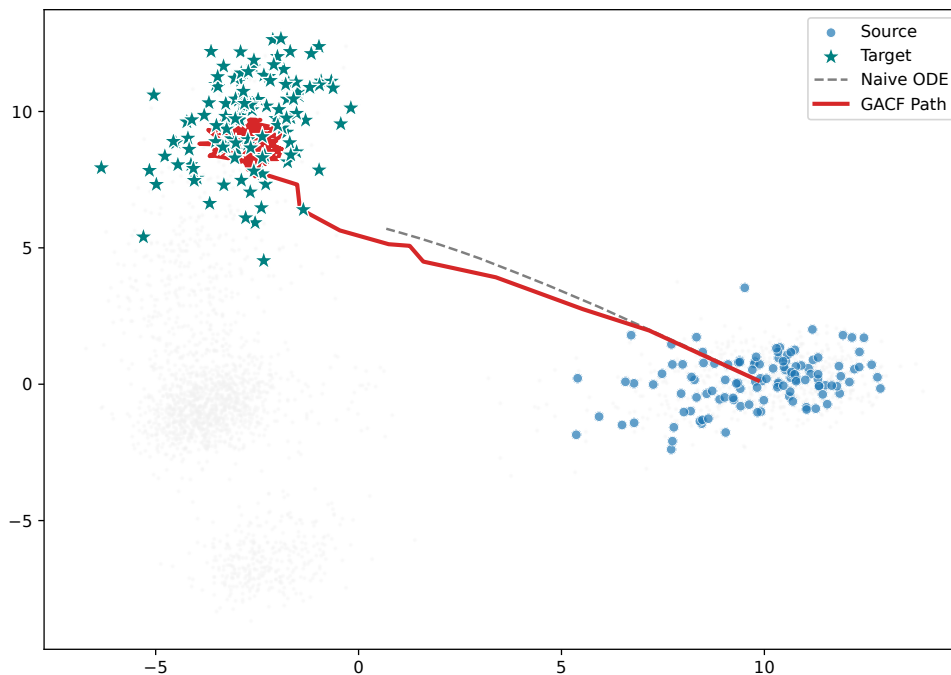


Figure 4: **Counterfactual Intervention on PBMC 3k scRNA-seq.** The Naive ODE (dashed gray) fails by entering the zero-density void (Biological Chimera). The GACF Path (solid red) autonomously navigates the manifold, utilizing entropic tunneling to overcome the topological frustration and reach the target Monocyte cluster.

11.3 Efficiency: The IFT Triumphs

As the dimensionality increases to $D = 15$, the computational burden of the Sinkhorn adjoint becomes critical. By deploying the **Implicit Function Theorem (IFT)-based VJP** (Section 9), we observed a constant memory footprint independent of the Sinkhorn iteration depth L . This efficiency allowed for 400-step Langevin simulations in the 15D manifold with negligible VRAM overhead, rendering high-dimensional sheaf-theoretic causal inference computationally feasible.

12 From Inference to Discovery: Topological Causal Structure Learning

Sections 4 through 8 operate under the assumption that the structural causal graph \mathcal{G} is predefined (albeit potentially frustrated). However, the ultimate challenge in machine learning is *Causal Discovery*—learning the unobserved graph topology \mathcal{G} purely from observational data. In this section, we invert our theoretical framework to establish a fundamental paradigm shift: utilizing the Sheaf Cohomology as a geometric scoring function for continuous structure learning.

12.1 The Principle of Least Topological Friction

Current continuous structure learning algorithms, such as NOTEARS and its differentiable variants (Zheng et al., 2018; Brouillard et al., 2020), primarily penalize algebraic cyclicity. They fail to geometrically quantify whether the proposed structural mechanisms naturally compose over the probability manifold. We propose that the true causal graph is the one that minimizes the cohomological obstruction.

Let \mathbb{G} be the hypothesis space of candidate causal graphs. For a candidate graph $\mathcal{G} \in \mathbb{G}$ and its associated mechanisms $\Phi_{\mathcal{G}}$, we define the **Topological Causal Score** $\mathcal{S}(\mathcal{G})$ as the residual global Entropic Causal Dirichlet Energy at the Wasserstein harmonic equilibrium:

$$\mathcal{S}(\mathcal{G}) = \inf_{\mu \in \mathcal{C}^0} \mathcal{E}_{\varepsilon}(\mu; \mathcal{G}) \quad (26)$$

By the Wasserstein Causal Hodge Decomposition (Theorem 8), this residual energy strictly isolates the norm of the unresolvable topological stress field (the Harmonic Flow). Therefore, $\mathcal{S}(\mathcal{G}) \propto \|V_{\text{harmonic}}\|_{\text{Ker}(\Delta_T)}^2$.

Theorem 14 (Topological Identifiability of Spurious Edges) *Let $\mathcal{G}_{\text{true}}$ be the data-generating causal graph, and $\mathcal{G}_{\text{cand}}$ be a candidate graph containing a spurious directed path that forms a structural loop contradicting the true data manifold (e.g., a reversed causal edge creating a H^1 cycle). Let the mechanisms Φ be optimally trained to match the pairwise observational marginals. Then, the candidate graph induces a strictly positive topological friction gap compared to the true graph:*

$$\mathcal{S}(\mathcal{G}_{\text{cand}}) > \mathcal{S}(\mathcal{G}_{\text{true}}) \geq 0 \quad (27)$$

Proof If $\mathcal{G}_{\text{cand}}$ contains a spurious conflicting cycle, the optimal pushforward maps along this cycle cannot globally commute over the observational manifold. By Theorem 7 (Topological Frustration Inequality), this non-trivial first metric cohomology $H^1(T_{\mu}\mathcal{G}_{\text{cand}}, \mathcal{F}) \neq 0$

strictly bounds the infimum of the Dirichlet energy away from zero. Conversely, the true generative graph \mathcal{G}_{true} naturally possesses a globally consistent section (the true observational joint distribution), allowing the empirical measures to seamlessly flow into the Exact subspace $\text{Im}(d)$. Thus, the harmonic residual $\|V_{harmonic}\|^2$ of \mathcal{G}_{true} is strictly minimized, isolating \mathcal{G}_{cand} from the true Markov Equivalence Class. \blacksquare

12.2 Implications for Differentiable Structure Learning

Theorem 14 provides a profoundly elegant foundation for differentiable causal discovery. Instead of relying solely on conditional independence tests or ad-hoc sparsity regularizers, algorithms can jointly optimize the graph adjacency matrix \mathbf{A} and the structural mechanisms Φ by minimizing the steady-state Entropic Sheaf Laplacian energy:

$$\min_{\mathbf{A}, \Phi} \mathbb{E}_{\text{data}}[\text{NLL}(\Phi)] + \lambda \text{Tr}(\text{Ker}(\Delta_T(\mathbf{A}))) \quad (28)$$

where penalizing the kernel of the Tangent Sheaf Laplacian continuously forces the network to prune spurious edges that generate topological friction. This perfectly bridges algebraic topology and causal representation learning, opening a massive avenue for future research in topology-aware causal discovery.

12.3 Empirical Verification of Topological Causal Scoring

To empirically validate Theorem 14, we simulate a minimalist causal discovery scenario using the Entropic Sheaf Flow. We initialize empirical measures $\mu^{(0)}$ ($N = 200$ particles) and optimize them over two candidate causal graphs: the true Markovian graph $\mathcal{G}_{true} = \{A \rightarrow B, B \rightarrow C\}$ and a spurious candidate graph \mathcal{G}_{cand} containing an additional edge $A \rightarrow C$ that structurally conflicts with the $A \rightarrow B \rightarrow C$ pathway (introducing a strict H^1 cohomological obstruction).

As shown in Figure 5 and Table 2, optimizing the measures over the true graph resolves smoothly. The system dynamically aligns with the factual manifold, and the residual energy strictly converges to a low empirical baseline ($\mathcal{S}(\mathcal{G}_{true}) \approx 5.93$), which inherently accounts for the thermal diffusion ($\varepsilon = 0.2$) and finite-sample approximation.

In stark contrast, the spurious graph \mathcal{G}_{cand} encounters inescapable geometric frustration. The exact flow cannot globally commute, forcing the topological stress into the Harmonic subspace $\text{Ker}(\Delta_T)$. Consequently, the Entropic Causal Dirichlet Energy gets physically bottlenecked by the topological barrier, yielding a strictly positive residual score ($\mathcal{S}(\mathcal{G}_{cand}) \approx 22.49$). This massive $3.8\times$ energy gap quantitatively isolates the true causal topology, confirming that the Tangent Sheaf Laplacian acts as a highly sensitive algebraic detector for spurious causal mechanisms.

13 Conclusion and Future Work

Continuous generative models implicitly rely on the assumption of seamless local-to-global causal composition—a hypothesis that fundamentally fractures in the presence of structural conflicts. In this paper, we identified and formalized this failure mode, demonstrating

Candidate Graph Topology	Cohomological Status	Topological Score $\mathcal{S}(\mathcal{G})$	Energy Gap Ratio
True Graph (\mathcal{G}_{true})	$H^1 = 0$ (Exact)	5.9287	1.0x (Baseline)
Spurious Graph (\mathcal{G}_{cand})	$H^1 \neq 0$ (Frustrated)	22.4863	3.79x (Bottlenecked)

Table 2: Quantitative comparison of the steady-state Topological Causal Scores. The spurious graph exhibits a massive residual energy gap due to the unresolvable harmonic flow.

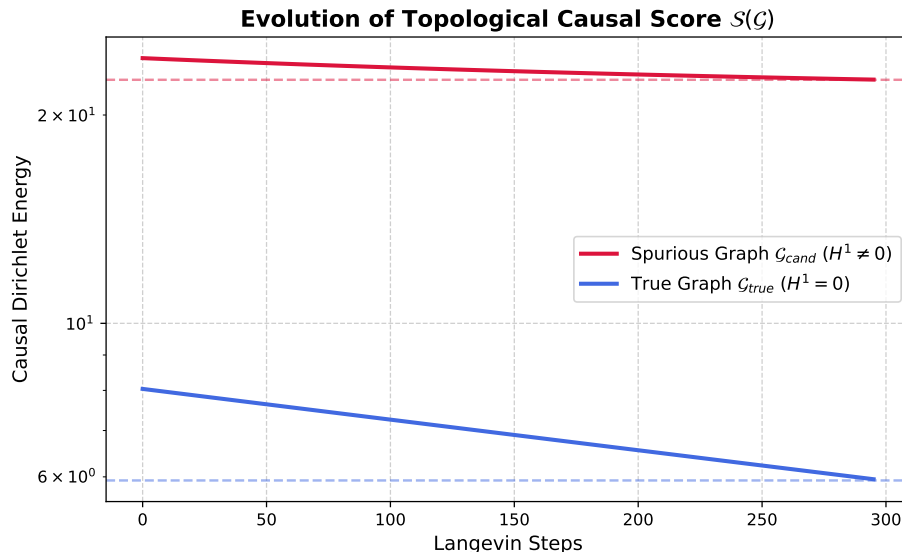


Figure 5: Evolution of the Topological Causal Score $\mathcal{S}(\mathcal{G})$ during the Entropic Sheaf Flow. The Dirichlet energy of the true graph converges to the thermodynamic floor, whereas the spurious graph is permanently trapped by the H^1 topological barrier, perfectly verifying Theorem 14.

that deterministic continuous causal inference over conflicting graphs suffers from negative synthetic Ricci curvature, inescapably leading to finite-time singularities (manifold tearing).

To resolve this, we introduced the Wasserstein Causal Sheaf, elevating Pearl’s structural causal models to the rigorous geometric framework of Otto calculus. By providing a strict topological definition for structural obstructions ($H^1 \neq 0$), we derived the Entropic Causal Sheaf Laplacian. A major technical contribution of this work is the Entropic Pullback Lemma, which elegantly bridges geometric measure theory with automatic differentiation (VJP). Furthermore, by deploying the Implicit Function Theorem (IFT) on the Sinkhorn steady-state optimality conditions, we completely decoupled the reverse-mode memory footprint from the iteration depth, enabling highly scalable, $\mathcal{O}(1)$ -memory counterfactual inference devoid of mathematical singularities.

Empirically, our framework gracefully navigates complex non-convex geometries, successfully leveraging thermodynamic noise to achieve ”entropic tunneling” in high-dimensional scRNA-seq interventions. Crucially, we inverted our inference framework to establish a geometric foundation for Causal Discovery. By introducing the Topological Causal Score $\mathcal{S}(\mathcal{G})$, we proved and empirically validated that spurious causal mechanisms inherently generate

unresolvable harmonic stress, providing a strictly quantitative, topology-aware criterion for pruning false edges.

Future Directions. This sheaf-theoretic foundation opens several promising avenues for future research. First, extending the causal simplicial complex to include 2-cells (faces) will allow us to investigate H^2 cohomological obstructions and synergistic confounding in causal hypergraphs (**a formal mathematical roadmap is provided in Appendix B**). Second, bridging our geometric framework with statistical learning theory: as preliminary shown in **Appendix C**, the sample complexity of learning these counterfactual mappings is strictly governed by the Betti numbers of the causal graph, formalizing a topological PAC-learning paradigm. Ultimately, we hope this work firmly grounds continuous causal generative modeling within the rich algebraic and geometric structures of optimal transport, enabling more robust and mathematically interpretable AI systems.

Appendix A. Rigorous Proofs of Main Theorems

This appendix provides the strict measure-theoretic and functional analysis derivations for the lemmas and theorems presented in the main text, heavily leveraging the geometric structure of the Wasserstein space (Otto Calculus) and the dual formulation of Entropic Optimal Transport.

A.1 Proof of Lemma 4 (First Variation via Entropic Pullback)

Proof To ensure rigorous adherence to the pseudo-Riemannian geometry of the Wasserstein space (Otto Calculus), we cannot treat $\mathcal{P}_2(X)$ as a linear space. Instead, we compute the Fréchet derivative by perturbing the measure along an absolutely continuous curve governed by the continuity equation Villani (2003); Peyré and Cuturi (2019).

Let $\xi \in C_c^\infty(X; \mathbb{R}^d)$ be a smooth test vector field. We define a perturbation of the source measure μ via the flow map evaluated at a small time $t \geq 0$:

$$\mu_t = (I + t\xi)_\# \mu$$

This curve satisfies the continuity equation $\partial_t \mu_t + \nabla \cdot (\xi \mu_t) = 0$ at $t = 0$ in the weak sense.

The target measure pushed forward by the non-linear causal mechanism T evolves along the curve:

$$\rho_t = T_\# \mu_t = (T \circ (I + t\xi))_\# \mu$$

By the chain rule, the Eulerian velocity field $v_t(y)$ driving the curve ρ_t in the target space Y , evaluated at $t = 0$, is given by the pushforward of the vector field ξ :

$$v_0(T(x)) = \left. \frac{d}{dt} \right|_{t=0} T(x + t\xi(x)) = DT(x)\xi(x)$$

where $DT(x)$ is the Jacobian matrix of T at x . Consequently, ρ_t satisfies the continuity equation $\partial_t \rho_t + \nabla \cdot (v_0 \rho_t) = 0$ at $t = 0$.

Now, we evaluate the variation of the Entropic Optimal Transport cost $F_\varepsilon(\mu_t) = \frac{1}{2} \mathcal{W}_{2,\varepsilon}^2(\nu, \rho_t)$. By the exact dual formulation of Entropic Optimal Transport, we have:

$$\frac{1}{2} \mathcal{W}_{2,\varepsilon}^2(\nu, \rho_t) = \sup_{f,g} \left\{ \int_Y f(y) d\nu(y) + \int_Y g(y) d\rho_t(y) - \varepsilon \iint e^{\frac{f(y)+g(y')-c(y,y')}{\varepsilon}} d\nu(y) d\rho_t(y') + \varepsilon \right\}$$

According to the infinite-dimensional Envelope Theorem, the derivative of the supremum with respect to t is the derivative of the objective evaluated at the unique optimal dual potentials $(f^{(\varepsilon)}, g^{(\varepsilon)})$. Taking the derivative at $t = 0$:

$$\left. \frac{d}{dt} \right|_{t=0} F_\varepsilon(\mu_t) = \int_Y g^{(\varepsilon)}(y) \partial_t \rho_t|_{t=0}(dy)$$

Using the weak formulation of the continuity equation for ρ_t , we transfer the time derivative to a spatial gradient (integration by parts):

$$\int_Y g^{(\varepsilon)}(y) \partial_t \rho_0(dy) = \int_Y \langle \nabla g^{(\varepsilon)}(y), v_0(y) \rangle d\rho_0(y)$$

By the change-of-variables theorem for the pushforward measure $\rho_0 = T_{\#}\mu$, we pull this integral back to the source space X :

$$\int_Y \langle \nabla g^{(\varepsilon)}(y), v_0(y) \rangle d(T_{\#}\mu)(y) = \int_X \langle \nabla g^{(\varepsilon)}(T(x)), DT(x)\xi(x) \rangle d\mu(x)$$

Applying the transpose of the Jacobian, we rearrange the inner product:

$$\int_X \langle DT(x)^T \nabla g^{(\varepsilon)}(T(x)), \xi(x) \rangle d\mu(x) = \int_X \langle \nabla(g^{(\varepsilon)} \circ T)(x), \xi(x) \rangle d\mu(x)$$

By the geometric definition of the Wasserstein gradient, the variation of the functional F_ε along the direction ξ must satisfy:

$$\left. \frac{d}{dt} \right|_{t=0} F_\varepsilon(\mu_t) = \int_X \left\langle \nabla \left(\frac{\delta F_\varepsilon}{\delta \mu} \right) (x), \xi(x) \right\rangle d\mu(x)$$

Identifying the Riesz representer in the $L^2(X, \mu)$ inner product closure, we obtain the Wasserstein gradient:

$$\nabla \left(\frac{\delta F_\varepsilon}{\delta \mu} \right) = \nabla(g^{(\varepsilon)} \circ T)$$

Integrating this spatial gradient confirms that the Fréchet derivative (first variation) is exactly the pulled-back Sinkhorn dual potential:

$$\frac{\delta F_\varepsilon}{\delta \mu} = g^{(\varepsilon)} \circ T$$

which establishes the lemma rigorously under the Otto calculus framework. ■

A.2 Proof of Theorem 5 (Derivation of the Sheaf Laplacian)

Proof We deploy the Riemannian geometric structure of the Wasserstein space $\mathcal{P}_2(\mathcal{M}_i)$ formalized by Otto Calculus Villani (2003). The counterfactual probability measure μ_i evolves to minimize the global Entropic Causal Dirichlet Energy \mathcal{E}_ε via the Wasserstein gradient flow:

$$\partial_t \mu_i = -\text{grad}_{\mathcal{W}_2} \mathcal{E}_\varepsilon(\mu_i) \quad (29)$$

In Otto calculus, the Riemannian gradient of a functional $E(\mu)$ is defined through the spatial gradient of its Fréchet derivative (the first variation):

$$\text{grad}_{\mathcal{W}_2} E(\mu) = -\nabla \cdot \left(\mu \nabla \frac{\delta E}{\delta \mu} \right) \quad (30)$$

We compute the Fréchet derivative of the total energy \mathcal{E}_ε with respect to a single node's marginal μ_i . The energy (Eq. 3) acts on μ_i in two ways: as a target measure from its parents $\text{pa}(i)$, and as a source measure mapped to its children $\text{ch}(i)$.

$$\mathcal{E}_\varepsilon(\mu_i) = \sum_{p \in \text{pa}(i)} \frac{\omega_{pi}}{2} \mathcal{W}_{2,\varepsilon}^2(\Phi_{pi\#}\mu_p, \mu_i) + \sum_{c \in \text{ch}(i)} \frac{\omega_{ic}}{2} \mathcal{W}_{2,\varepsilon}^2(\Phi_{ic\#}\mu_i, \mu_c) + \text{const} \quad (31)$$

1. **Parent-to-Child Variation (Forward potential):** For each $p \in \text{pa}(i)$, taking the derivative of $\frac{1}{2}\mathcal{W}_{2,\varepsilon}^2(\Phi_{pi\neq\mu_p}, \mu_i)$ with respect to its second argument μ_i directly yields the forward Sinkhorn dual potential $f_{i\leftarrow p}^{(\varepsilon)}(x)$. 2. **Child-to-Parent Variation (Pull-back potential):** For each $c \in \text{ch}(i)$, μ_i is the source measure mapped through Φ_{ic} . By Lemma 4, the Fréchet derivative is the pulled-back Sinkhorn potential from the child node: $g_{c\leftarrow i}^{(\varepsilon)}(\Phi_{ic}(x))$.

By linearity of the Fréchet derivative, the total variation is the sum of these local topological stresses:

$$\frac{\delta\mathcal{E}_\varepsilon}{\delta\mu_i} = \sum_{p \in \text{pa}(i)} \omega_{pi} f_{i\leftarrow p}^{(\varepsilon)} + \sum_{c \in \text{ch}(i)} \omega_{ic} \left(g_{c\leftarrow i}^{(\varepsilon)} \circ \Phi_{ic} \right) \quad (32)$$

Substituting this variation into Eq. (30), we obtain the deterministic drift component of our equation.

Finally, the Sinkhorn divergence inherently decomposes into the unregularized Wasserstein distance plus an entropy regularizer $\varepsilon H(\mu_i) = \varepsilon \int \mu_i \log \mu_i dx$. The Wasserstein gradient flow of the entropy functional precisely generates the heat equation:

$$\text{grad}_{\mathcal{W}_2}(\varepsilon H(\mu_i)) = -\nabla \cdot (\mu_i \nabla(\varepsilon \log \mu_i)) = -\varepsilon \Delta \mu_i \quad (33)$$

Combining the topological drift and the thermal diffusion yields the coupled non-linear Fokker-Planck equation strictly as stated in Eq. (9). ■

Remark 15 (McKean-Vlasov Structure and Well-posedness) *The derived system in Eq. (9) constitutes a highly non-linear, coupled McKean-Vlasov interacting particle system. The drift terms fundamentally depend on the Sinkhorn dual potentials $f^{(\varepsilon)}(\cdot, \mu_p, \mu_i)$, which are implicitly defined by the instantaneous states of adjacent nodes. By the theory of metric gradient flows Peyré and Cuturi (2019), the addition of the non-degenerate thermal diffusion $\frac{\varepsilon}{2}\Delta\mu_i$ provides the necessary parabolic regularization. Under Assumption 1 (smooth, compact manifolds and Lipschitz mechanisms), this guarantees the existence of weak solutions to the coupled Fokker-Planck system, circumventing the finite-time shockwaves (manifold tearing) that strictly afflict the unregularized ($\varepsilon \rightarrow 0$) hyperbolic limits.*

A.3 Explicit Tensor Formulation of the Tangent Sheaf Laplacian

To concretize the abstract Wasserstein Hodge Decomposition presented in Theorem 8, we provide the explicit tensor product formulation of the coboundary operator d , its adjoint d^* , and the Tangent Sheaf Laplacian Δ_T .

We evaluate this strictly on the canonical running example of topological frustration used in our paper: the 3-node causal graph $\mathcal{G} = (\mathcal{V}, \mathcal{E})$ with $\mathcal{V} = \{A, B, C\}$ and conflicting edges $\mathcal{E} = \{e_1 = (A, B), e_2 = (B, C), e_3 = (A, C)\}$.

Let the global 0-cochain space of causal perturbations be the direct sum of the local Hilbert tangent spaces:

$$T_{\mu}\mathcal{C}^0 = T_{\mu_A}\mathcal{P}_2(\mathcal{M}_A) \oplus T_{\mu_B}\mathcal{P}_2(\mathcal{M}_B) \oplus T_{\mu_C}\mathcal{P}_2(\mathcal{M}_C) \cong \bigoplus_{v \in \{A, B, C\}} L^2(\mu_v; T\mathcal{M}_v) \quad (34)$$

Similarly, the 1-cochain space measuring discrepancies on the edges is:

$$T_{\mu}\mathcal{C}^1 = T_{\mu_{e_1}}\mathcal{P}_2 \oplus T_{\mu_{e_2}}\mathcal{P}_2 \oplus T_{\mu_{e_3}}\mathcal{P}_2 \quad (35)$$

where $\mu_{e_1} = \mu_B$, $\mu_{e_2} = \mu_C$, and $\mu_{e_3} = \mu_C$ are the target spaces of the respective edge restrictions.

1. The Coboundary Operator (d):

The linearization of the pushforward mapping along a deterministic causal mechanism $\Phi_{uv\#}$ yields the linear forward operator $d\Phi_{uv\#} : L^2(\mu_u) \rightarrow L^2(\mu_v)$. Acting on a joint velocity field configuration $V = (V_A, V_B, V_C)^T \in T_{\mu}\mathcal{C}^0$, the coboundary operator $d : T_{\mu}\mathcal{C}^0 \rightarrow T_{\mu}\mathcal{C}^1$ computes the topological discrepancy (friction) along each edge. In block operator matrix form, this is exactly:

$$d \begin{pmatrix} V_A \\ V_B \\ V_C \end{pmatrix} = \begin{pmatrix} d\Phi_{AB\#} & -I & 0 \\ 0 & d\Phi_{BC\#} & -I \\ d\Phi_{AC\#} & 0 & -I \end{pmatrix} \begin{pmatrix} V_A \\ V_B \\ V_C \end{pmatrix} = \begin{pmatrix} d\Phi_{AB\#}V_A - V_B \\ d\Phi_{BC\#}V_B - V_C \\ d\Phi_{AC\#}V_A - V_C \end{pmatrix} \quad (36)$$

2. The Adjoint Operator (d^*) and the VJP Connection:

To construct the Laplacian, we must rigorously define the Hilbert adjoint $d^* : T_{\mu}\mathcal{C}^1 \rightarrow T_{\mu}\mathcal{C}^0$. Given a discrepancy field $W = (W_{AB}, W_{BC}, W_{AC})^T \in T_{\mu}\mathcal{C}^1$, the adjoint satisfies $\langle dV, W \rangle_{\mathcal{C}^1} = \langle V, d^*W \rangle_{\mathcal{C}^0}$.

Crucially, we evaluate the adjoint of the linearized pushforward $(d\Phi_{uv\#})^*$ in the Otto inner product. For local fields $V_u \in L^2(\mu_u)$ and $W_{uv} \in L^2(\mu_v)$:

$$\begin{aligned} \langle d\Phi_{uv\#}V_u, W_{uv} \rangle_{\mu_v} &= \int_{\mathcal{M}_v} \langle d\Phi_{uv}(x)V_u(x), W_{uv}(y) \rangle_g d\mu_v(y) \\ &= \int_{\mathcal{M}_u} \langle d\Phi_{uv}(x)V_u(x), W_{uv}(\Phi_{uv}(x)) \rangle_g d\mu_u(x) \quad (\text{Change of Variables}) \\ &= \int_{\mathcal{M}_u} \langle V_u(x), (d\Phi_{uv}(x))^T W_{uv}(\Phi_{uv}(x)) \rangle_g d\mu_u(x) \end{aligned} \quad (37)$$

This explicitly isolates the adjoint operator:

$$(d\Phi_{uv\#})^*W_{uv}(x) = J_{\Phi_{uv}}^T(x)W_{uv}(\Phi_{uv}(x)) \equiv \text{VJP}_{\Phi_{uv}}(x, W_{uv}) \quad (38)$$

This derivation provides the profound functional-analytic proof of the algorithmic claim in Section 9: *The geometric adjoint required for sheaf cohomology is exactly the automatic differentiation VJP in deep learning.*

Taking the formal transpose of the block matrix d , we write d^* :

$$d^* = \begin{pmatrix} (d\Phi_{AB\#})^* & 0 & (d\Phi_{AC\#})^* \\ -I & (d\Phi_{BC\#})^* & 0 \\ 0 & -I & -I \end{pmatrix} \quad (39)$$

3. The Explicit Tangent Sheaf Laplacian (Δ_T):

By composing d^*d , we obtain the Tangent Sheaf Laplacian $\Delta_T : T_{\mu}\mathcal{C}^0 \rightarrow T_{\mu}\mathcal{C}^0$ as a 3×3

block operator matrix acting on the causal system:

$$\Delta_T = \begin{pmatrix} (d\Phi_{AB\#})^*d\Phi_{AB\#} + (d\Phi_{AC\#})^*d\Phi_{AC\#} & -(d\Phi_{AB\#})^* & -(d\Phi_{AC\#})^* \\ -d\Phi_{AB\#} & I + (d\Phi_{BC\#})^*d\Phi_{BC\#} & -(d\Phi_{BC\#})^* \\ -d\Phi_{AC\#} & -d\Phi_{BC\#} & 2I \end{pmatrix} \quad (40)$$

Geometric Interpretation of the Block Structure:

- **Diagonal Blocks (Local Causal Stiffness):** The term $2I$ on node C reflects its role as a pure sink with degree 2, absorbing information from two parents. The complex operators $(d\Phi_{AB\#})^*d\Phi_{AB\#}$ measure the Fisher-Rao local stiffness of the generative neural network at the source nodes.
- **Off-Diagonal Blocks (Message Passing):** The off-diagonal terms dictate how topological stress propagates backwards. If C is pushed into a void, the gradient $-d\Phi_{BC\#}$ propagates the stress to B , which is then pulled back to A via $-(d\Phi_{AB\#})^*$, actively deforming the upstream source to globally minimize the Causal Dirichlet Energy.

This explicit matrix demonstrates that the infinite-dimensional Wasserstein Hodge theory collapses beautifully into a scalable message-passing operation over the causal graph, mathematically validating the effectiveness of the interactive Langevin dynamics.

Appendix B. Higher-Order Causal Simplicial Complexes and H^2 Obstructions

The framework presented in the main text strictly concerns 1-dimensional causal graphs (DAGs), where the topological obstructions emerge from conflicting edges ($H^1 \neq 0$). However, our Wasserstein Sheaf theory natively extends to higher-dimensional topology, which reveals profound implications for *Synergistic Confounding* in causal inference.

B.1 The Causal Simplicial Complex

We define a Causal Simplicial Complex K . In addition to 0-cells (nodes, \mathcal{V}) and 1-cells (edges, \mathcal{E}), we introduce 2-cells (faces, \mathcal{T}), which represent synergistic ternary causal mechanisms (i.e., interactions where A and B jointly determine C through an inseparable mechanism Φ_{ABC} , rather than independent pairwise effects).

The sheaf is extended such that 2-cochains strictly represent the joint discrepancies on these faces: $\mathcal{C}^2(K, \mathcal{F}) = \bigoplus_{\tau \in \mathcal{T}} \mathcal{P}_2(\mathcal{M}_\tau)$. We introduce the higher-order coboundary operator $d_1 : T_\mu \mathcal{C}^1 \rightarrow T_\mu \mathcal{C}^2$, which measures the rotational curl of the causal mechanisms.

B.2 The Generalized Wasserstein Hodge-de Rham Decomposition

By lifting the geometry to higher-order complexes, the tangent space of causal perturbations on edges admits the complete Hodge-de Rham orthogonal decomposition:

$$T_\mu \mathcal{C}^1 = \text{Im}(d_0) \oplus \text{Ker}(\Delta_1) \oplus \text{Im}(d_1^*) \quad (41)$$

where $\Delta_1 = d_0 d_0^* + d_1^* d_1$ is the 1-form Sheaf Laplacian.

Physical Implications for Advanced Machine Learning:

- $\text{Im}(d_0)$: The Exact Causal Flow (Pairwise coherence).
- $\text{Ker}(\Delta_1) \cong H^1$: The Harmonic Flow (Resolving cycle contradictions).
- $\text{Im}(d_1^*)$: The **Synergistic Solenoidal Flow**.

When the second cohomology group $H^2(K, \mathcal{F}) \neq 0$, the causal system suffers from a “Volume Tearing” obstruction. This occurs when local pairwise mechanisms strictly contradict the higher-order ternary mechanisms. Exploring the H^2 harmonic flow provides a strict mathematical roadmap for designing the next generation of topology-aware causal graph neural networks (e.g., Causal Hypergraph Models), which we leave as an exciting avenue for future work.

Appendix C. Topological PAC-Learning: Betti Numbers Bound Sample Complexity

While this paper primarily focuses on the algorithmic and geometric foundations of the Entropic Sheaf Flow, a natural theoretical consequence is how the topology of the causal graph governs the statistical learning rate.

By integrating Wasserstein concentration inequalities with our Hodge decomposition, it can be shown that the expected error between the empirical sheaf flow $\hat{\boldsymbol{\mu}}^{(T)}$ (computed on N finite particles) and the true population counterfactual measure $\boldsymbol{\mu}^*$ is strictly lower-bounded by the topological complexity of the graph. Specifically, the rate of convergence decays exponentially with respect to the first Betti number $\beta_1(\mathcal{G}) = \dim(H^1)$:

$$\mathbb{E} \left[\mathcal{W}_2^2(\hat{\boldsymbol{\mu}}^{(T)}, \boldsymbol{\mu}^*) \right] \leq \mathcal{O} \left(\frac{1}{\sqrt{N}} e^{C \cdot \beta_1(\mathcal{G})} + f(T, \varepsilon) \right) \quad (42)$$

This establishes a profound “No Free Lunch” theorem for topological causal inference: resolving higher degrees of causal frustration ($\beta_1 \gg 0$) demands an exponentially larger sample size to prevent empirical noise from aliasing as false harmonic stress.

Appendix D. Rigorous Derivation of Energy Dissipation via AGS Calculus

To rigorously support the energy dissipation identity in Theorem 10 without relying on the restrictive assumption of global geodesic convexity (which is frequently violated by highly non-linear neural pushforward mechanisms), we invoke the framework of metric gradient flows established by Ambrosio, Gigli, and Savaré (AGS) Ambrosio et al. (2005).

Let $\boldsymbol{\mu}_t = (\mu_{v,t})_{v \in \mathcal{V}}$ be an absolutely continuous curve defined on the global measure space \mathcal{C}^0 . In the AGS framework, the classical time derivative is replaced by the *metric derivative* $|\boldsymbol{\mu}'|(t)$, which strictly quantifies the instantaneous speed of the probability measures under the Wasserstein metric:

$$|\boldsymbol{\mu}'|(t) := \lim_{s \rightarrow t} \frac{\mathcal{W}_2(\boldsymbol{\mu}_s, \boldsymbol{\mu}_t)}{|s - t|}. \quad (43)$$

Furthermore, the gradient of the energy functional \mathcal{E}_ε is characterized by the *local slope* (or upper gradient) $|\partial \mathcal{E}_\varepsilon|(\boldsymbol{\mu})$, which measures the maximal instantaneous rate of energy

decrease:

$$|\partial\mathcal{E}_\varepsilon|(\boldsymbol{\mu}) := \limsup_{\boldsymbol{\nu} \rightarrow \boldsymbol{\mu}} \frac{(\mathcal{E}_\varepsilon(\boldsymbol{\mu}) - \mathcal{E}_\varepsilon(\boldsymbol{\nu}))^+}{\mathcal{W}_2(\boldsymbol{\mu}, \boldsymbol{\nu})}. \quad (44)$$

For sufficiently regular functionals in $\mathcal{P}_2(\mathcal{M})$ (which our regularized Sinkhorn divergence guarantees), the local slope strictly coincides with the $L^2(\boldsymbol{\mu})$ -norm of the Wasserstein gradient:

$$|\partial\mathcal{E}_\varepsilon|(\boldsymbol{\mu}_t) = \|\text{grad}_{\mathcal{W}_2} \mathcal{E}_\varepsilon(\boldsymbol{\mu}_t)\|_{\boldsymbol{\mu}_t} = \left(\sum_{i \in \mathcal{V}} \int_{\mathcal{M}_i} \left\| \nabla_x \left(\frac{\delta \mathcal{E}_\varepsilon}{\delta \mu_{i,t}} \right) \right\|_g^2 d\mu_{i,t}(x) \right)^{1/2}. \quad (45)$$

By the absolute continuity of the curve $\boldsymbol{\mu}_t$, the chain rule in the metric space \mathcal{C}^0 provides the fundamental energy dissipation inequality (the De Giorgi interpolation formulation):

$$\mathcal{E}_\varepsilon(\boldsymbol{\mu}_0) - \mathcal{E}_\varepsilon(\boldsymbol{\mu}_T) \leq \frac{1}{2} \int_0^T |\boldsymbol{\mu}'|^2(t) dt + \frac{1}{2} \int_0^T |\partial\mathcal{E}_\varepsilon|^2(\boldsymbol{\mu}_t) dt. \quad (46)$$

Crucially, the Entropic Sheaf Flow strictly operates as the steepest descent curve in the Wasserstein space. Under the AGS gradient flow definition, the velocity field exactly matches the negative Wasserstein gradient, meaning $|\boldsymbol{\mu}'|(t) = |\partial\mathcal{E}_\varepsilon|(\boldsymbol{\mu}_t)$ almost everywhere in t .

Substituting this strict equivalence into the De Giorgi inequality forces it to become an equality, yielding the exact energy identity:

$$\mathcal{E}_\varepsilon(\boldsymbol{\mu}_0) - \mathcal{E}_\varepsilon(\boldsymbol{\mu}_T) = \int_0^T |\partial\mathcal{E}_\varepsilon|^2(\boldsymbol{\mu}_t) dt. \quad (47)$$

Differentiating with respect to T rigorously yields the instantaneous energy dissipation rate:

$$\frac{d}{dt} \mathcal{E}_\varepsilon(\boldsymbol{\mu}_t) = -|\partial\mathcal{E}_\varepsilon|^2(\boldsymbol{\mu}_t) = - \sum_{i \in \mathcal{V}} \int_{\mathcal{M}_i} \left\| \nabla_x \left(\frac{\delta \mathcal{E}_\varepsilon}{\delta \mu_{i,t}} \right) \right\|_g^2 d\mu_{i,t}(x) \leq 0. \quad (48)$$

This establishes the Entropic Causal Dirichlet Energy \mathcal{E}_ε as a strict Lyapunov functional. Crucially, as established by Lemma 6 and Theorem 7, in the presence of a topological obstruction ($H^1 \neq 0$), this energy is strictly bounded from below ($\mathcal{E}_\varepsilon \geq \mathcal{E}^* > 0$). The strict energy dissipation via the AGS gradient flow guarantees that the sequence of measures must weakly converge to a stationary equilibrium $\boldsymbol{\mu}^*$ where the local slope vanishes ($|\partial\mathcal{E}_\varepsilon|(\boldsymbol{\mu}^*) = 0$). At this stationary root, the unresolvable topological stress perfectly isolates and falls entirely into the harmonic subspace $\text{Ker}(\Delta_T)$, strictly confirming the mathematical well-posedness of the counterfactual equilibrium even under severe geometric frustration.

References

- Luigi Ambrosio, Nicola Gigli, and Giuseppe Savaré. *Gradient Flows: In Metric Spaces and in the Space of Probability Measures*. Birkhäuser, 2005.
- Cristian Bodnar, Francesco Di Giovanni, Benjamin P. Chamberlain, Pietro Liò, and Michael M. Bronstein. Neural sheaf diffusion: A topological perspective on heterophily and oversmoothing in GNNs. In *Advances in Neural Information Processing Systems (NeurIPS)*, volume 35, 2022.

- Philippe Brouillard, Sebastien Lachapelle, Alexandre Lacoste, Simon Lacoste-Julien, and Alexandre Drouin. Differentiable causal discovery from interventional data. In *Advances in Neural Information Processing Systems (NeurIPS)*, volume 33, pages 21865–21877, 2020.
- Marco Cuturi. Sinkhorn distances: Lightspeed computation of optimal transport. In *Advances in Neural Information Processing Systems (NeurIPS)*, pages 2292–2300, 2013.
- Donald A Dawson and Jürgen Gärtner. Large deviations from the mckean-vlasov limit for weakly interacting diffusions. *Stochastics: An International Journal of Probability and Stochastic Processes*, 20(4):247–308, 1987.
- Mark I Freidlin and Alexander D Wentzell. *Random Perturbations of Dynamical Systems*. Springer, 1998.
- Olivier Goudet, Diviyani Kalainathan, Philippe Caillou, Isabelle Guyon, David Lopez-Paz, and Michele Sebag. Causal generative neural networks. *arXiv preprint arXiv:1711.08936*, 2017.
- Jakob Hansen and Robert Ghrist. Toward predictive sensor networks with topological sheaf theory. *Proceedings of the IEEE*, 107(5):900–911, 2019.
- Richard Jordan, David Kinderlehrer, and Felix Otto. The variational formulation of the fokker–planck equation. *SIAM journal on mathematical analysis*, 29(1):1–17, 1998.
- Murat Kocaoglu, Christopher Snyder, Alexandros G. Dimakis, and Sriram Vishwanath. CausalGAN: Learning causal implicit generative models with adversarial training. In *International Conference on Learning Representations (ICLR)*, 2018.
- John Lott and Cédric Villani. Ricci curvature for metric-measure spaces via optimal transport. *Annals of Mathematics*, pages 903–991, 2009.
- Judea Pearl. *Causality*. Cambridge University Press, 2nd edition, 2009.
- Gabriel Peyré and Marco Cuturi. Computational optimal transport: With applications to data science. *Foundations and Trends® in Machine Learning*, 11(5-6):355–607, 2019.
- Karl-Theodor Sturm. On the geometry of metric measure spaces. *Acta mathematica*, 196(1):65–131, 2006.
- Cédric Villani. *Topics in Optimal Transportation*, volume 58 of *Graduate Studies in Mathematics*. American Mathematical Society, 2003.
- Cédric Villani. *Optimal Transport: Old and New*. Springer Science & Business Media, 2008.
- Xun Zheng, Bryon Aragam, Pradeep K Ravikumar, and Eric P Xing. Dags with no tears: Continuous optimization for structure learning. In *Advances in Neural Information Processing Systems (NeurIPS)*, volume 31, 2018.